Modeling 2D Spatio-Tactile Population Receptive Fields of the Fingertip in Human Primary Somatosensory Cortex

Susanne Stoll,[1,2,3,8,10*] Falk Luesebrink,[3,4,5] D. Samuel Schwarzkopf,[6,9] Hendrik Mattern,[3,4,7] Peng Liu,[1,2,3,10] Johanna Noelle,[2,3] and Esther Kuehn[1,2,3,7,10]

[1]Hertie Institute for Clinical Brain Research, Tuebingen, Germany

[2]Institute for Cognitive Neurology and Dementia Research, Otto-von-Guericke University Magdeburg, Germany

[3]German Center for Neurodegenerative Diseases, Magdeburg, Germany

[4]Biomedical Magnetic Resonance, Otto-von-Guericke-University Magdeburg, Germany

[5]Nuclear Magnetic Resonance Methods & Development Group, Max Planck Institute for Human Cognitive and Brain Sciences, Leipzig, Germany

[6]School of Optometry and Vision Science, The University of Auckland, New Zealand

[7]Center for Behavioral Brain Sciences, Magdeburg, Germany

[8]Max Planck Institute for Biological Cybernetics, Tuebingen, Germany

[9]Experimental Psychology, University College London, United Kingdom

[10]German Center for Neurodegenerative Diseases, Tuebingen, Germany

*Correspondence: stollsus@gmail.com

Keywords: functional magnetic resonance imaging, population receptive field modeling, ultra-high field, 7T, spatial, tactile, primary somatosensory cortex, human, exploratory research, simulations

Abstract: Tactile fingertip sensations are critical for everyday life. Accordingly, tactile fingertip maps have been extensively studied in human primary somatosensory cortex. However, the fine-grained functional architecture of these maps remains largely unknown. To uncover this architecture, we sought to estimate 2D spatio-tactile population receptive fields (pRFs) of the tip of the index finger in human Brodmann area 3b (BA3b). Using functional magnetic resonance imaging at 7T and submillimeter resolution along with prospective motion correction, we recorded brain responses whilst participants sensed a row of vibrotactile pins sweeping along cardinal axes over a portion of the fingertip. To estimate pRF position and size, we initially fit a 2D Gaussian pRF

model to the data, which, however, produced largely implausible pRF estimates. Simulations indicated that this likely occurred because the size of pRFs in BA3b surpasses the portion of the fingertip we stimulated, resulting in an incomplete mapping of pRFs. To address this issue, we constrained the fitting procedure and refined the 2D Gaussian pRF model by keeping pRF size constant. Our results for pRF position then revealed that the ulnar-to-radial axis spanning the fingertip maps onto a superior-to-inferior axis in BA3b. Both the putatively large pRF size (relative to the mapping area) and the pRF position gradient we uncover here appear compatible with receptive field properties quantified in monkeys. Our study provides the first comprehensive investigation into the fine-grained functional architecture of human fingertip maps and brings us one step closer to a thorough understanding thereof.

1 Introduction

Day in, day out, we use our fingertips for a variety of touch-based tasks, such as twisting a cap, pressing a lever, tapping on a pad, popping a pimple, or stroking someone else's face. In fact, by guiding both our perception and motor actions, tactile fingertip sensations render our interaction with the world incredibly effective. This becomes most evident when such sensations are suddenly impaired following (temporary) paresthesia, disease, injury, or amputation (e.g., Gorniak et al., 2014; Kawaiah et al., 2020; Nora et al., 2004). Yet, despite the functional significance of fingertip sensations for our daily lives, we know surprisingly little about how tactile input to the fingertips is represented in the human brain. More precisely, although we know that human primary somatosensory cortex (SI) represents our fingertips in a somatotopic fashion (for a review, see Janko et al., 2022), we lack insights into the fine-grained architecture of an individual fingertip representation.

The building blocks of this fine-grained architecture are tactile neurons and their 2D spatial receptive fields – the region on the skin a tactile neuron is sensitive to. To investigate spatial receptive field properties of the fingertips at the level of neuronal populations, a plethora of studies has combined functional magnetic resonance imaging (fMRI) at 7T with phase-encoding analyses (Engel, 2012; Engel et al., 1994; Kuehn et al., 2018; P. Liu et al., 2021; Puckett & Sanchez-Panchuelo, 2023; Puckett et al., 2020; Sanchez-Panchuelo et al., 2010; Sanchez-Panchuelo et al., 2018). This is because fMRI at an ultra-high field strength ($\geq$ 7T) allows for high image resolution whilst ensuring a good signal-to-noise ratio of the fMRI response, which is thought to help resolve small somatotopic gradients in individual brains (Puckett & Sanchez-Panchuelo, 2023).

For phase-encoded fingertip mapping, participants' fingertips (or a subregion thereof) are typically successively stimulated vibro-tactilely and voxel-wise blood-oxygen-level-dependent (BOLD) time courses recorded simultaneously. Assuming neurons in different voxels have receptive fields preferentially encoding different fingertips, the stimulus-evoked responses in these time courses should vary systematically in their delay. As such, a sine wave can be fit to each time course to obtain a

phase estimate reflecting this delay[1] and thus which voxel responds preferentially to which fingertip (Engel, 2012; Engel et al., 1994; Puckett & Sanchez-Panchuelo, 2023). Using this approach, the existence of so-called between-fingertip maps has been repeatedly demonstrated, where the tips of the thumb, index, middle, ring, and little finger are typically represented somatotopically along an inferior-to-superior axis in Brodmann area (BA) 3b, 1, and 2 in SI (Kuehn et al., 2018; P. Liu et al., 2021; Puckett et al., 2020; Sanchez-Panchuelo et al., 2010; Sanchez-Panchuelo et al., 2018). Notably, such maps have also been reported for other experimental designs, analysis techniques, stimulus types, and lower field strengths (3T, 4T) as well as for multi-focal stimulation along the fingers and finger tapping instead of passive tactile stimulation (for a review, see Janko et al., 2022).

A more explicit way to investigate spatial receptive field properties at the level of neuronal populations is fMRI-based population receptive field (pRF) modeling (Dumoulin & Knapen, 2018; Dumoulin & Wandell, 2008). A pRF refers to the aggregate receptive field properties of a population of neurons within a voxel (see Figure 1; Dumoulin & Knapen, 2018; Dumoulin & Wandell, 2008). Similar to phase-encoding analyses (Engel, 2012; Engel et al., 1994), pRF modeling has been pioneered in the field of vision science to study retinotopic maps in the human brain (Dumoulin & Knapen, 2018; Dumoulin & Wandell, 2008). However, unlike phase-encoding analyses, pRF modeling typically uses biological encoding models inspired by invasive electrophysiology to estimate pRF properties (Dumoulin & Knapen, 2018; Naselaris et al., 2011). As such, pRF modeling makes explicit assumptions about how a stimulus interacts with the pRF of a voxel over time to obtain predicted BOLD time courses, which are then compared to actually observed BOLD time courses (Dumoulin & Knapen, 2018; Dumoulin & Wandell, 2008). A perfect pRF model can thus – at least in theory – provide an exhaustive functional characterization of a certain brain region (Naselaris et al., 2011).

In vision science, pRFs are typically modeled as a 2D excitatory Gaussian function, which allows the center position (x_0, y_0) and size (σ) of a pRF to be estimated in 2D sensory space (see Figure 1; Dumoulin & Knapen, 2018; Dumoulin & Wandell, 2008). To adapt 2D pRF modeling to the case of 1D between-fingertip stimulation, the 2D Gaussian model can be either constrained by keeping one dimension constant (e.g., fixing y_0) or reduced to a 1D Gaussian pRF model (e.g., removing y_0). A series of high-resolution 7T-fMRI studies adopting such approaches did not only show that pRF position maps in SI are reminiscent of between-fingertip maps typically obtained via phase estimates, but also that overall pRF size might differ between different digits, although individual results did not always converge (P. Liu et al., 2021; Puckett et al., 2020; Schellekens et al., 2021). What these studies leave completely unaddressed, though, is how neighboring points on a given fingertip and thus the skin's 2D receptor sheet maps onto human SI (see Figure 1; Sereno et al., 2022).

Unlike research in humans, research in owl and/or macaque monkeys involving invasive single-neuron or multi-unit recordings already started tackling this question (Merzenich et al., 1978; Nelson et al., 1980; Sur et al., 1980). Using dense tactile stimulation delivered via fine glass probes, this line of

[1] E.g. via a Fourier transform or cross-correlation procedure.

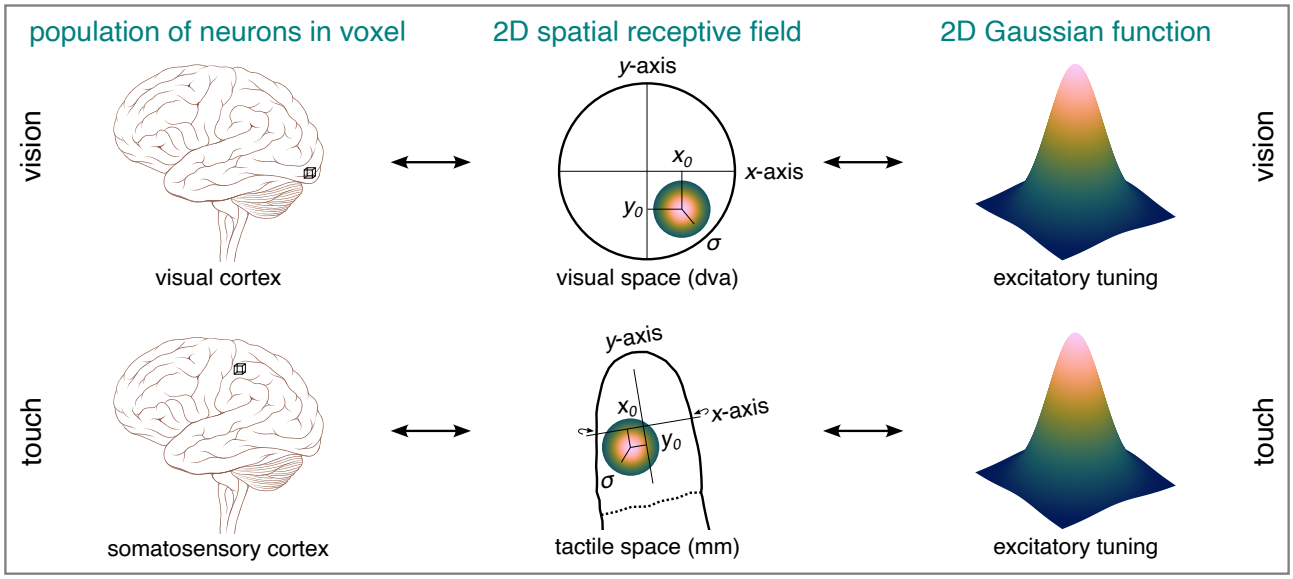

Figure 1. **2D spatial pRF.** A 2D spatio-visual pRF refers to the 2D region on the retina and thus visual space a population of neurons within a voxel (and most likely beyond) is sensitive to when visually stimulated. A 2D spatio-tactile pRF of the fingertip refers to the 2D region on the fingertip skin and thus tactile space a population of neurons within a voxel (and most likely beyond) is sensitive to when tactiley stimulated. Both types of pRFs can be modeled as an excitatory 2D Gaussian function, where x_0 and y_0 coordinates represent its center position and σ its size in sensory space (i.e., a Cartesian coordinate system). Wrap-around arrows indicate an x-axis that is slightly wrapped around the fingertip. pRF = population receptive field. dva = degrees of visual angle. The brain insets are adapted from *Brain human lateral view*, by P. J. Lynch, 2006, Wikimedia (https://commons.wikimedia.org/wiki/File:Brain_human_lateral_view.svg). CC BY 2.5.

work revealed that excitatory 2D receptive fields are organized so that the ulnar-to-radial and the distal-to-proximal axis spanning a monkey's finger(tip) are represented along a superior-to-inferior and anterior-to-posterior axis in BA3b, respectively (Merzenich et al., 1978; Nelson et al., 1980). It furthermore indicated that the area of excitatory receptive fields in BA3b can range from a subportion of to almost the entire fingertip (Merzenich et al., 1978; Nelson et al., 1980; Sur et al., 1980). Interestingly, a series of human fMRI studies differing along various methodological dimensions (experimental design, analysis technique, stimulus type, field strength, image resolution, digits of interest) has already investigated the representation of the distal-to-proximal axis along the fingers in BA3b. Whereas some findings point to an ordered mapping just like in monkeys (Blankenburg et al., 2003; Choi et al., 2016; Sanchez-Panchuelo et al., 2012), others are less clear (P. Liu et al., 2025; Overduin & Servos, 2004, 2008; Schweisfurth et al., 2014, 2015). However, the granularity of stimulation in all these studies was coarse (no more than two effective locations per phalange) and the ulnar-to-radial axis along individual fingers was not mapped, rendering it impossible to fully resolve the fine-grained architecture of an individual fingertip representation.

In the present exploratory study, we therefore sought to estimate fine-grained, excitatory 2D pRFs of the fingertip in human BA3b (see Figure 1). To maximize sensitivity, we combined 7T-fMRI at submillimeter resolution with prospective motion correction (PMC; Maclaren et al., 2012; Stucht et al., 2015) and precision neuroscience (Gordon et al., 2017). Whereas PMC refers to correcting head motion at the time of data acquisition, precision neuroscience refers to collecting a large amount of data per individual for a detailed characterization of individual brains. To map 2D spatio-tactile pRFs, we recorded BOLD responses whilst participants sensed a fine-grained row of vibrotactile pins moving along cardinal axes over a portion of the tip of the index finger. To estimate 2D pRFs,

we fit an excitatory 2D Gaussian pRF model to the data. To refine our modeling procedure and investigate the reliability, explanatory power, computational validity (accuracy), and meaningfulness of our results, we furthermore performed reliability, cross-validation, and simulation analyses. Our study provides the first comprehensive investigation into the intricate architecture of an individual fingertip representation in the human brain.

2 Methods

2.1 Participants

The study sample comprised 3 healthy participants (2 female, 1 male; age range: 27-39 years; all right-handed; all authors) referred to as subject 01, 02, and 03 (Sub-01, Sub-02, and Sub-03). Two of them were highly experienced magnetic resonance imaging (MRI) participants. None of them were naïve as to the purpose of the experiment. All participants were screened for contraindications for 7T-(f)MRI and PMC, gave written informed consent prior to participating in the experiment, and reported intact sensory and motor function of their hands. All participants furthermore gave explicit written informed consent that their pseudonymized brain data can be shared publicly without any form of defacing. Experimental procedures were approved by the Ethics Committee of the Otto-von-Guericke University (OVGU) Magdeburg.

2.2 Apparatus

A whole-body MAGNETOM 7T-MRI scanner (7T Classic; Siemens Healthineers, Erlangen, Germany) along with a 32-channel head coil (Nova medical, Wilmington, MA, USA) was used to acquire functional and anatomical images at the MRI Research Infrastructure of the OVGU Magdeburg. For participants' comfort, a blank display was projected onto a screen at the back of the MRI scanner. Participants viewed the screen through a mirror mounted onto the head coil. Participants' head was stabilized via foam padding wrapped around the entire back part of their head (from cheek bone to cheek bone). An MRI-compatible piezostimulator developed by QuaeroSys (https://www.quaerosys.com/) was used to stimulate a portion of the tip of the left index finger (glabrous skin) via a single stimulation module comprising 16 vibrotactile pins. These pins had a pointy pinhead (maximal diameter: $\sim$1 mm; distance from pin center to pin center: $\sim$2.5 mm), were arranged as a 4$\times$4 array (see Figure 2), and passed through a surface containing 16 circular apertures. The piezostimulator had a voltage output of 4096 levels representing the possible range of pin heights. A dark surgical marker was used to draw the 4$\times$4 pin array onto participants' fingertips (see 2.4 Procedure) and an elongated cushion to stabilize the left hand.

Head motion was corrected online via a PMC system consisting of an MRI-compatible camera (Metria Innovation, Milwaukee, Wisconsin, USA) with a lighting unit illuminating a marker with

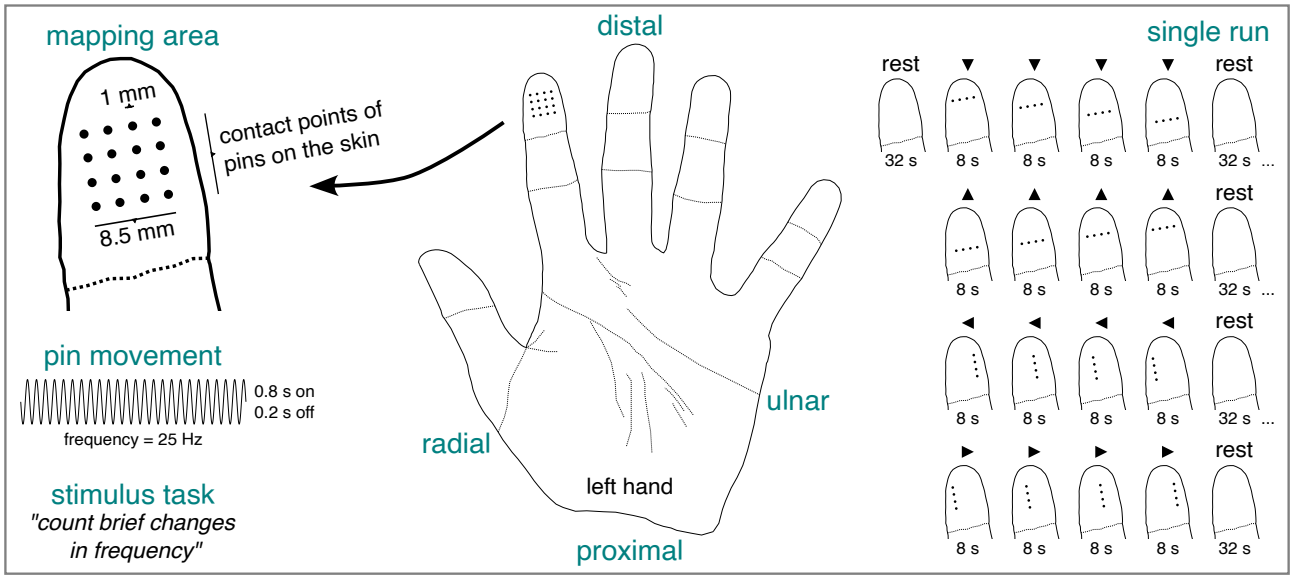

Figure 2. **Spatio-tactile pRF mapping experiment.** The mapping area consisted of an array of vibrotactile pins placed on a portion of the tip of the left index finger. In any given run, participants sensed a row of pins moving along cardinal axes interspersed with baseline (rest) periods. The pins oscillated according to a sine wave with alternating on and off periods. Participants were required to count brief changes in frequency of the sine wave throughout a given run. Black arrowheads indicate the movement direction of the pins. pRF = population receptive field.

Moiré patterns (size: 15×15 mm^2). The camera including lighting unit was mounted onto the MRI bore's ceiling above the head coil and tracked the marker with a sampling rate of 86 Hz. The marker was attached to the extending bit of an MRI-compatible customized mouthpiece that was worn by participants during scanning. The customized mouthpieces were manufactured at the University Clinic for Oral and Maxillofacial Surgery in Magdeburg, covered 6 teeth of the upper jaw (i.e., the central and lateral incisors and the canines), and ensured rigid coupling between the marker and participants' head. The video stream captured by the camera was sent to a dedicated computer that processed the image frames and estimated head motion along 6 degrees of freedom: 3 rotation axes (pitch, roll, yaw) and 3 translation axes (forward-back, up-down, left-right). These estimates were then forwarded to the MRI scanner and converted from the camera's coordinate system to the scanner's coordinate system via a precalibrated transformation matrix. The PMC system tracks motion with a precision of $\sim$ 0.01 mm (translation) and $\sim$ 0.01° (rotation), which is more than an order of magnitude smaller than the voxel edge length. More details on the PMC system and its validation can be found in Maclaren et al. (2012) and Stucht et al. (2015).

2.3 Stimuli

The pRF mapping area consisted of an array of vibrotactile pins that was divided into 4 horizontal and 4 vertical bars, each comprising 4 pins, resulting in 8 stimulus positions. A single bar therefore functioned as the pRF mapping stimulus. The pins of this bar stimulus typically oscillated according to a sine wave with a constant frequency ($A = 3095$; $f = 25$ Hz; $\omega = 157.08$ rad/s; $\varphi = 4.71$ rad). However, as part of an oddball task (see 2.4 Procedure), the bar stimulus occasionally oscillated according to a sine wave with a lower frequency ($A = 3095$; $f = 10$ Hz; $\omega = 62.83$ rad/s; $\varphi = 4.71$ rad). For an illustration of the pRF mapping area and stimulus, see Figure 2. To account for an

accumulation of small temporal delays in the order of several seconds over the course of a full run of the pRF mapping experiment, we occasionally dropped points sampled from the sine wave. The bar stimulus used here can be seen as the tactile equivalent of bar stimuli comprising flickering high-contrast images frequently adopted for visual pRF modeling (e.g., Alvarez et al., 2015; Dumoulin & Wandell, 2008).

2.4 Procedure

Adhering to the principles of precision neuroscience (Gordon et al., 2017), we collected a large amount of data for each participant. In particular, the pRF mapping experiment consisted of 4 sessions $\grave{a}$ 10 runs per participant. For each participant, these 4 sessions were split across 2 days (either consecutive or 1 day apart), so that session 1-2 were conducted on the first day and session 3-4 on the second day. There was a break of ∼15-30 min between sessions on the same day, during which participants were taken out of the MRI scanner. At the beginning of each session, a series of prescans (localizer, transmit adjustment, and shimming) was acquired, followed by anatomical data, followed by functional BOLD data for the pRF mapping experiment and a series of additional scans (see 2.5 MRI acquisition).

At the beginning of each pRF mapping run, 4 dummy volumes were acquired. Next, the bar stimulus translated step-by-step along a portion of the tip of the left index finger. Specifically, it translated from distal-to-proximal (32 s), proximal-to-distal (32 s), ulnar-to-radial (32 s), and radial-to-ulnar (32 s) with a baseline interval (32 s) before/after every sweep. During the dummy volumes and the baseline interval, no stimulation was applied. Note that baseline intervals are necessary for estimating large pRFs (Dumoulin & Knapen, 2018; Dumoulin & Wandell, 2008). Each bar position was stimulated for 8 s. To prevent adaptation, pin oscillation was ceased for 0.2 s every 0.8 s. Moreover, to ensure sustained attention, participants were asked to detect 0-10 oddball events throughout each run. They were instructed to count these events and verbally report whether there were more than 5 oddballs at the end of a given run. The number and timing of oddball events in any given run was determined randomly. During an oddball event, the frequency of the sine wave changed briefly for 0.2 s (see 2.3 Stimuli). For an illustration of the pRF mapping experiment, see Figure 2.

Prior to the start of the first scanning session on a given day, the camera had to warm up for ∼1 hr. During this time, we performed 1-2 mock pRF runs. Moreover, before the start of each pRF mapping run, a subset of pins was supposed to rise and fall once and participants were asked to report if this was not the case. These check-ups were conducted to ensure that all components of the stimulation equipment were intact and the experiment could run through properly. Nonetheless, due to the relatively large number of runs collected in any given session, it could happen that the pRF mapping experiment did not run through properly, which was clearly perceivable (e.g., pins stopped oscillating). As such, participants were instructed to report such instances at the end of a given run, in which case this run was repeated. Similarly, a run was repeated whenever participants

reported that they were "inattentive" or "sleepy" at the end of the run. Per participant and session, the range of invalid and thus to-be-repeated runs was 0-3.

Prior to the start of session 1, participants performed a training session outside the MRI scanner, where they familiarized themselves with the pRF mapping experiment and the oddball task. All participants were able to correctly report the movement direction of the bar stimulus, to detect the oddball events, and perceive each bar position clearly and distinctly. To ensure consistent placement of the pins in each session, we aligned the lower edge of the surface element of a second (identical) stimulation module with the terminal finger joint, and used a dark surgical marker to draw the 4×4 pin array onto each participant's fingertip. If not actively washed off, the drawing could remain on the fingertip for several days. Moreover, to ensure that the pins remained in the same position throughout a whole scanning session, the stimulation module was attached to the index finger using medical tape. Participants were furthermore instructed to keep still during scanning and to refrain from moving their hand and fingers in particular. An overview of system environments and software tools adopted in the pRF mapping experiment can be found in Table S1. This table also covers visualizations presented in 1 Introduction and 2 Methods.

2.5 MRI acquisition

After localizing participants' brains, we calibrated the transmit voltage, followed by head shimming to make the main magnetic field (B0) more homogenous. Subsequent to these prescans, we acquired whole-brain anatomical images using a T1-weighted 3D magnetization-prepared rapid acquisition with gradient echo (MPRAGE) sequence (Mugler & Brookeman, 1990, see Table 1). We then mapped geometric distortions induced by residual B0 field inhomogeneities via the point-spread-function (PSF) method (In & Speck, 2012; In et al., 2015; Zaitsev et al., 2004). Afterwards, we acquired several runs of functional BOLD images for pRF mapping (see 2.4 Procedure). In both cases (geometric distortions and pRF), we used a T2$*$-weighted 2D echo planar imaging (EPI) sequence (see Table 1). Between the first and second run of functional data acquisition, we additionally mapped geometric distortions using the T2$*$-weighted 2D EPI sequence for acquiring functional data with reversed phase-encoding as well as a T2$*$-weighted 2D gradient-echo sequence with two different echo times. However, these additional images were only acquired for potential future investigations and not used in the scope of the present study.

For acquiring functional images for pRF mapping and mapping geometric distortions, the image slab was centered at the base of the hand knob (i.e., a posteriorly-oriented hook when viewed sagittally; Yousry et al., 1997) and then titled so that the anterior-posterior midline of the slab (the longer line of symmetry) was aligned with an oblique axis at approximately $160/340^{\circ}$. Moreover, any acquired dummy volumes (see 2.4 Procedure) were directly discarded by the MRI scanner. As for the MPRAGE sequence, the motion estimates obtained via the PMC system were used to update the field-of-view prior to the excitation of each individual k-space line. As for the EPI sequences, this was done prior to the excitation of all k-space lines pertaining to an individual slice. As such, for

Table 1
Parameters of Main Scanning Sequences

Characteristics	3D MPRAGE	2D EPI	2D EPI (PSF)
Number of slices	224	30	30
Slice orientation	sagittal	t tilted twds. c	t tilted twds. c
Slice order		interleaved	interleaved
Voxel size	0.8 mm iso	0.9 mm iso	0.9 mm iso
TR	2.5 s	2 s	2 s
TE	2.45 ms	20 ms	20 ms
TI	1050 ms		
Flip angle	5°	76°	90°
PI	GRAPPA	GRAPPA	GRAPPA
Acceleration factor	2	4	4
Ref. lines for PI	32	64	64
BW	320 Hz/pixel	1072 Hz/pixel	1072 Hz/pixel
FoV	218×218×179.2 mm	200×200×27 mm	200×200×27 mm
Echo spacing	5.8 ms	1.08 ms	1.06 ms
Image interpolation		zero filling	
Phase partial Fourier		5/8	5/8
Number of volumes	1	144	1
PSF reduced FoV factor			4
EPI-PSF acceleration factor			1
EPI-PSF reference lines			8

Note. Blank entries denote "not applicable". TR = repetition time. TE = echo time. TI = inversion time. Ref. = reference. PI = parallel imaging. BW = bandwidth. FoV = field-of-view. PSF = point-spread function. EPI = echo planar imaging. MPRAGE = magnetization-prepared rapid acquisition with gradient echo. iso = isotropic. GRAPPA = generalized autocalibration partial parallel acquisition. t = transversal. twds. = towards. c = coronal.

both anatomical and functional data, PMC accounted for head motion within but not between runs or sessions. The distortion correction of the functional images using the PSF method was performed online via a fully-automated procedure. All acquired images were exported in DICOM format. The entire sequence protocol is publicly available (see Data and code availability).

2.6 Preprocessing

We designed a customized preprocessing pipeline that aligns and coregisters anatomical and functional images across all 4 sessions without manual intervention and constructs an anatomical surface model for each participant. The input data for this pipeline were the anatomical and distortion-corrected functional DICOM images that had been prospectively corrected for within-run motion (see 2.5 MRI acquisition). As a first step, we removed invalid functional runs (see 2.4 Procedure) as well as the first volume of each functional run which was the reference volume for distortion correction. We then converted all remaining functional and anatomical DICOM images to NIfTI format and formatted the data according to the Brain Imaging Data Structure (BIDS; Gorgolewski et al., 2016).

As for the anatomical images of each session, we subsequently downsampled these to match the resolution of the functional images (interpolation method: cubic), B1-bias-field-corrected them via unified segmentation adjusted for high-resolution 7T data (Ashburner & Friston, 2005; Lüsebrink et al., 2017, 2021), and finally masked them using a deep learning strategy for skull-stripping[2] (Hoopes et al., 2022). To obtain an initial masked anatomical template across sessions, we then aligned these masked anatomical images (interpolation method: nearest neighbor[3]) and calculated the median across them (Lüsebrink et al., 2017, 2021). To obtain an unmasked anatomical template across sessions, we furthermore applied the resulting transformation matrices to the unmasked bias-field-corrected anatomical images, thus bringing them in alignment (interpolation method: nearest neighbor), and calculated the median across them [4]. To obtain a final masked anatomical template across sessions[5], we masked this unmasked anatomical template by using a deep learning strategy for skull-stripping (Hoopes et al., 2022). The final masked anatomical template was used for coarse coregistration purposes (see below). The unmasked anatomical template was used for reconstructing an anatomical cortical surface model[6] (Dale et al., 1999; Fischl, 2012; Fischl et al., 1999). As part of the reconstruction process, we adopted a deep learning strategy for generating a brain mask (Hoopes et al., 2022). A subset of the reconstructed anatomical surfaces was later converted from surface to MAT format (along with the vertex-wise functional time series, see below). Lastly, we derived cytoarchitectonic labels using a probabilistic atlas (Fischl et al., 2008) including labels for right and left BA3b as well as anatomical labels using the gyral-based Desikan-Killiany cortical atlas including labels for right and left postcentral gyrus, that is, the location of SI (Desikan et al., 2006).

As for the functional images of each session, we first averaged across all images of a given run. Next, we generated a brain mask by thresholding these run-wise functional averages, obtaining the largest component (to remove non-brain tissue), and morphologically closing holes (due to noise/imperfect thresholding). Subsequently, we used these run-wise brain masks to mask the run-wise average functional images. All masked run-wise average functional images were then used to generate a masked functional template across sessions by aligning these images (interpolation method: nearest neighbor) and calculating the median across them. The final masked anatomical template (see above) was then coregistered to this masked functional template[7] (interpolation method: nearest neighbor). Next, we applied both resulting types of transformation matrices to every functional image of each run in one go[8] (interpolation method: nearest neighbor), therefore aligning them and coregistering them to the final masked anatomical template. More specifically, we used the forward transformation

[2]This strategy is known to be accurate and robust (Hoopes et al., 2022).

[3]Here and elsewhere, nearest neighbor interpolation was used to keep spatial blurring minimal.

[4]This two-step procedure counteracts alignment issues that can arise when generating an unmasked anatomical template across sessions directly due to non-brain tissue.

[5]The final masked anatomical template was generated because masking a template (instead of generating it from already masked images) should be more precise.

[6]The usage of an anatomical template (with a reduced level of noise due to averaging; Lüsebrink et al., 2017, 2021) instead of a single anatomical image is known to facilitate the construction of the surface model for anatomical data at submillimeter resolution (Tian, Bilgic, et al., 2021; Tian, Zaretskaya, et al., 2021).

[7]This approach was adopted because it is easier to register whole-brain data to partial-brain data (instead of vice versa) especially when non-brain tissue is being removed.

[8]This reduces the number of interpolation steps and thus interpolation artifacts.

matrices for generating the masked functional template and the inverse of the transformation matrix for coregistering the final masked anatomical template to the masked functional template. This first coarse coregistration step was used as a seed for a second fine coregistration step, where we coregistered every coarsely-coregistered functional image of each run to the unmasked anatomical template (interpolation method: nearest neighbor) using the previously generated cortical surface model and boundary-based registration[9] (BBR; Greve & Fischl, 2009; Polimeni et al., 2018). Lastly, we used the transformation matrices resulting from BBR to project the coarsely-coregistered functional data onto the cortical surface model, thus resampling them to surface vertices. To this end, we used the voxel in the functional image that was located midway (projection fraction $= 0.5$) between corresponding vertices on the gray-white matter and pial boundary[10]. Moreover, we modestly smoothed the data along the surface[11] (surface FWHM $= 1$ mm). The resulting vertex-wise functional time series for each run (henceforth fMRI time series) were then converted from MGH to MAT format before undergoing linear-detrending and z-standardization. For an overview of the preprocessing steps, see Figure S1. The preprocessing pipeline including data after BIDS formatting are publicly available (see Data and code availability). For adopted system environments and software tools as well as additional notes, see Table S1.

2.7 Data analysis

2.7.1 Functional localization

To localize stimulus-evoked activity in SI, we performed a simple vertex-wise general linear model (GLM) analysis for each participant and brain hemisphere. The input data were the preprocessed vertex-wise fMRI time series for session 1 concatenated across 10 runs. The GLM comprised a constant boxcar regressor for each stimulus position (4 horizontal bars and 4 vertical bars) convolved with a canonical hemodynamic response function (HRF; The FIL Methods Group, 2021) and a constant term for each run. Baseline intervals were modeled implicitly (Pernet, 2014). We computed t-statistic maps for the contrast stimulation vs baseline (rest): [1 1 1 1 1 1 1 1 0 0 0 0 0 0 0 0 0 0]. Contrasting stimulation vs rest is known to result in an increase in differential brain activity in stimulated and decrease in non-stimulated cortical sites in contralateral primary sensory areas, such as primary visual cortex (Shmuel et al., 2002; Stoll et al., 2020) and SI (Tal et al., 2017). Ipsilaterally, however, a wide-spread decrease of differential brain activity is typically observed in these areas (Shmuel et al., 2002; Tal et al., 2017).

[9] Boundary-based registration aligns a cortical surface reconstruction (based on a high-quality image with good anatomical contrast) to the gray-white matter boundary in the functional data (with a rather minimal amount of gray-white contrast; Greve & Fischl, 2009; Polimeni et al., 2018). As such, it is well-suited for surface-based pRF modeling relying on accurate positioning of the cortical surface model relative to the functional data (Polimeni et al., 2018). It is also known to excel at aligning partial-brain functional data to whole-brain anatomical data (Greve & Fischl, 2009).

[10] This approach was adopted to reduce partial volume effects and the effect of large draining veins residing on the pial surface (Bause et al., 2020; Koopmans et al., 2010; Polimeni et al., 2010).

[11] This served to reduce noise.

2.7.2 Delineations

To delineate fingertip clusters, we superimposed the label for postcentral gyrus and BA3b onto the unthresholded t-statistic maps rendered onto a spherical cortical surface model of the right brain hemisphere. Next, we visually identified clusters of increased brain activity (t-statistic > 0) falling entirely into the postcentral gyrus label and falling entirely into or overlapping the BA3b label. We then manually delineated the extent of these clusters.

2.7.3 PRF modeling

To estimate spatio-tactile pRFs per participant and brain hemisphere, we performed a pRF modeling analysis using all 30 runs of session 2-4[12]. Moreover, to conduct a split-half reliability analysis and cross-validation analyses, we repeated this analysis for the 15 odd-numbered and the 15 even-numbered runs of session 2-4. In each case, we first averaged the preprocessed vertex-wise fMRI time series across all runs of interest[13]. We then fit three pRF models to the averaged data. The first model consisted of a 2D excitatory Gaussian function (henceforth 2dg model) with 5 free parameters: pRF center position (x_0, y_0), pRF size (σ), pRF baseline (β_0), and pRF amplitude (β_1). The second model consisted of a 2D excitatory Gaussian function where the parameter for pRF size was fixed ($\sigma = 8.5$ mm; henceforth 2dg-fix model), leaving 4 free parameters (x_0, y_0, β_0, β_1). The third model was a model without any spatial tuning and thus 2 free parameters (β_0, β_1), essentially consisting of a boxcar function reflecting the presence or absence of tactile stimulation (henceforth onoff model). For both the 2dg and the 2dg-fix model, we expressed pRF center position and pRF size in physical units (mm) and estimated pRF center position in a Cartesian coordinate system where origin corresponded to the midpoint of the mapping area on the left fingertip (i.e., the pin array). For an illustration of the pRF modeling pipeline, see Figure 3.

For all three models, we first predicted an fMRI time series. To this end, we calculated an overlap image by multiplying an image of the pRF model and a binarized image of the stimulus per volume (a stimulus movie). These images consisted of a 170×170 pixel matrix, where 1 pixel corresponded to 0.05 mm on the skin. For each overlap image, we then aggregated the pixel values by calculating the mean percent overlap with the image of the pRF model, resulting in a predicted neuronal time series. This neuronal time series was then convolved with a canonical HRF (The FIL Methods Group, 2021, see also 2.7.1 Functional localization), resulting in a predicted fMRI time series. For the 2dg model, we generated 8750 predictions by sampling all putative parameter combinations from a 3D search space for pRF position and size (x_0, $y_0 =$ from -10.625 to $+10.625$ mm with 25 evenly-spaced values; $\sigma =$ from 0 to 12.75 mm with 15 evenly-spaced values and 0 being excluded). For the 2dg-

[12]This means the data involved in functional localization and delineation (see 2.7.1 Functional localization and 2.7.2 Delineations) were independent of those involved in pRF modeling, thus circumventing issues of circularity (e.g., Kriegeskorte et al., 2009; Stoll et al., 2022).

[13]It has been shown that averaging is particularly beneficial for heavily noise-tainted fMRI data both in terms of goodness-of-fit and accuracy of pRF parameter estimates (Senden et al., 2014), such as 7T-fMRI data at submillimeter resolution.

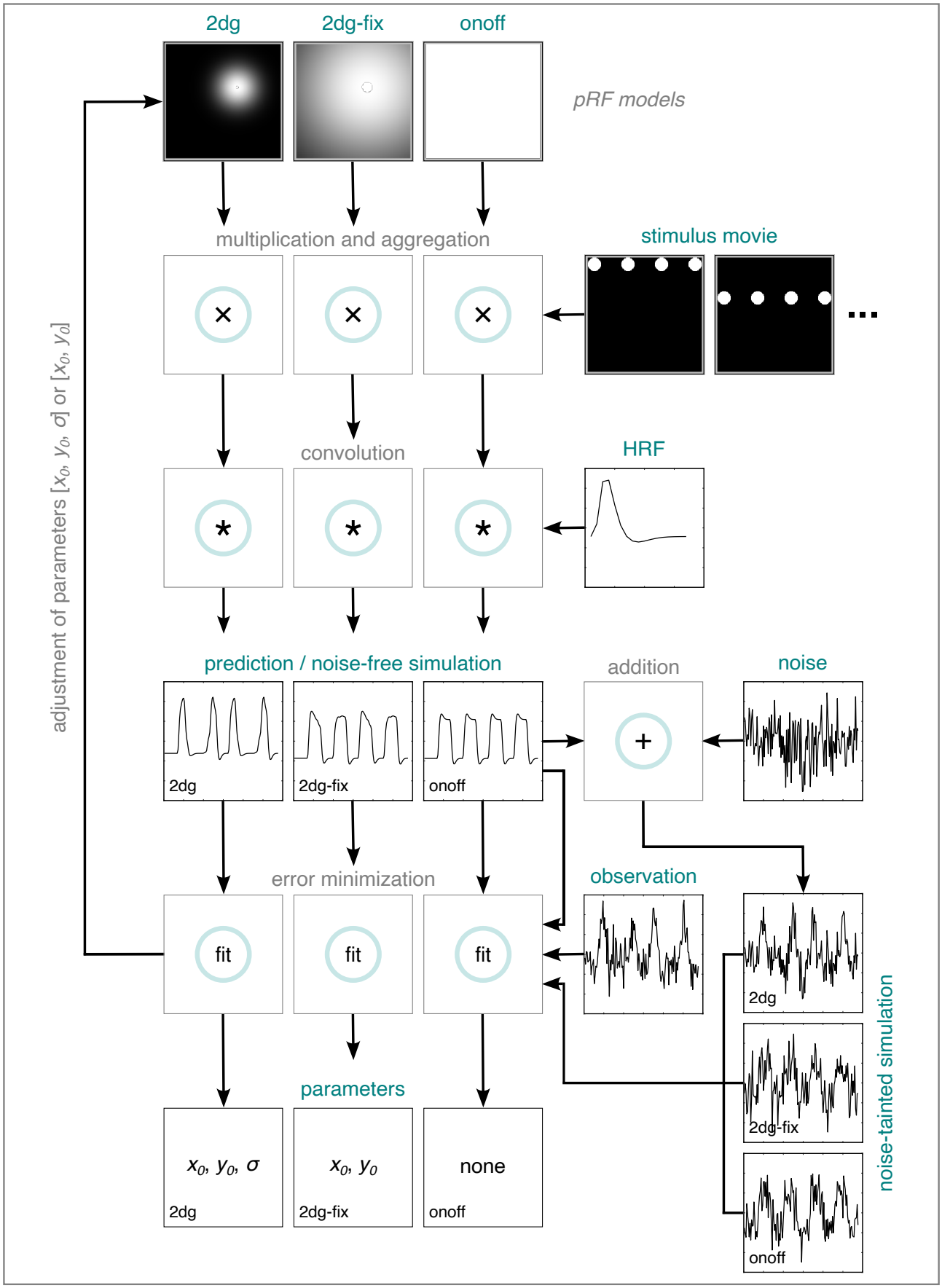

Figure 3. **PRF modeling pipeline.** *PRF modeling for empirically-observed data*: A pRF model, a stimulus movie, and an HRF are used to predict an fMRI time series, which is then compared to an empirically-observed fMRI time series. This is repeated many times by varying the parameters of the pRF model (if there are any). The parameters producing the best fit (lowest error between predicted and observed time series) are retained. *PRF modeling for simulated data*: The components for predicting an fMRI time series are used to simulate a noise-free fMRI time series. Depending on the purpose of the simulation, this noise-free fMRI time series remains as it is or is repeatedly perturbed by noise. The noise-free or noise-tainted time series are then fed into the pRF modeling pipeline as if they represented empirically-observed data. HRF = hemodynamic response function. 2dg = 2D Gaussian pRF model with unconstrained optimization. 2dg-fix = 2D Gaussian pRF model with parameter for pRF size fixed and constrained grid search. onoff = pRF model without any spatial tuning that simply reflects the presence or absence of tactile stimulation. pRF = population receptive field. fMRI = functional magnetic resonance imaging.

fix model, we generated 625 predictions by sampling from the same search space but dropping the dimension for pRF size because pRF size was fixed for this model. For the onoff model, we generated a single prediction. We then determined the Pearson correlation between the predicted and observed fMRI time series. For the 2dg and the 2dg-fix model, we subsequently selected the combination of parameter values showing the largest goodness-of-fit (squared Pearson correlation, R^2) as final pRF estimates. Only for the 2dg model, this constrained grid search fit was followed by an unconstrained optimization procedure taking the grid search fits as seeds and using a Nelder-Mead algorithm to further maximize the goodness-of-fit (Lagarias et al., 1998; Nelder & Mead, 1965). This is because the 2dg model with unconstrained optimization resulted in largely implausible parameter estimates (see 3.2 Fingertip pRFs in BA3b are larger than the mapping area). To address this issue, we introduced the 2dg-fix model with a constrained grid search and based all further analyses on this model. And finally, to estimate β_1 and β_0, we performed linear regression between the observed and the predicted fMRI time series representing the final fit for each model.

To validate the explanatory power of our results, we conducted a 2-fold-cross-validation analysis where the goodness-of-fit for pRF parameter estimates obtained for the odd runs was calculated using the even runs (first cross-validation fold) and vice versa (second cross-validation fold) for both the 2dg-fix model and the onoff model. To investigate whether the 2dg-fix model has superior explanatory power over the onoff model, we compared the cross-validated goodness-of-fit (cR^2) per vertex for this model to the cross-validated goodness-of-fit for the onoff model. This is possible because the cross-validation procedure we apply here automatically accounts for model complexity. And lastly, to determine how much the overall explanatory power varies between participants and models, we extracted all vertices falling within a given delineated BA3b cluster (see 2.7.2 Delineations) and determined the median cross-validated goodness-of-fit for each participant and model.

2.7.4 Simulations

To investigate the implausibility, computational validity (e.g., Lerma-Usabiaga et al., 2020; Senden et al., 2014; Zeidman et al., 2018), and meaningfulness of our pRF estimates, we performed a series of simulations. The basic principle underlying these simulations consists in simulating a noise-free fMRI time series for a specific pRF model by following the steps for predicting an fMRI time series (see 2.7.3 PRF modeling and Figure 3). Depending on the type of simulation, this time series either remains as it is or is perturbed by random Gaussian noise and z-scored afterwards, resulting in a noise-tainted fMRI time series. Next, a specific pRF model is fit to the simulated noise-free or noise-tainted time series by feeding the time series into the pRF modeling pipeline as if it represented truly observed data (see 2.7.3 PRF modeling and Figure 3).

Implausibility To investigate why fitting a 2dg model with unconstrained optimization resulted in implausible pRF estimates (see 3.2 Fingertip pRFs in BA3b are larger than the mapping area), we simulated how well we can recover the parameters of ground-truth pRFs varying in size when we add

or do not add noise to the simulated data. This allowed us to test for the hypothesis that for large pRFs surpassing the mapping area, there is not enough unique information left in a noise-tainted time course to keep the parameter estimates within a plausible range. In a noise-free time course, however, this information is present, resulting in accurate recovery irrespective of pRF size. As such, using the 2dg model, we first simulated noise-free time courses for ground-truth pRFs with a center position at origin ($x_0 = 0$ mm; $y_0 = 0$ mm) and 6 different sizes ($\sigma = 1.0625$, 2.125, 3.1875, 4.25, 6.375, 8.5 mm). We then perturbed each of these time courses 100000 times with random Gaussian noise ($\sigma_{noise} = 2$, expressed in units of mean percent overlap with the pRF model). Next, we fit a 2dg model with unconstrained optimization to both the noise-free and noise-tainted time courses. For each ground-truth pRF in the noise-tainted case, we then calculated the median as well as the 1st and 99th percentile over the 100000 repeats, individually for each pRF parameter (x_0, y_0, σ).

Computational validity To computationally validate the 2dg-fix model with constrained grid search, we simulated how well we can recover the parameters of ground-truth pRFs varying in center position when we add or do not add noise to the data. Whereas the latter allows us to identify flaws in our adapted pRF fitting pipeline, the former permits us to approximate the accuracy of empirical pRF estimates. To this end, we first used the 2dg-fix model to simulate noise-free time courses for pRFs with 25 different x_0 positions (from -10.625 to +10.625 mm with 25 evenly-spaced values) and 25 different y_0 positions (from -10.625 to +10.625 mm with 25 evenly-spaced values), matching all 625 search grid value pairs (see 2.7.3 PRF modeling and Figure 7, upper left panel). We then selected a subset of these time courses (i.e., the 4th, 8th, 12th, 16th and 20th value out of the 25 x_0 and y_0 positions, respectively), reflecting 25 different search grid value pairs (see Figure 8, upper panel), and perturbed each of these time courses 100000 times with random Gaussian noise ($\sigma_{noise} = 2$, expressed in units of mean percent overlap with the pRF model). We did this twice to simulate an odd and even dataset. Next, we fit the 2dg-fix model with constrained grid search to both the simulated noise-free and noise-tainted time courses of each dataset. In the noise-tainted case, we then determined the number of times (out of 100000) the constrained grid search resulted in a specific grid search value pair for a given ground-truth pRF, separately for each dataset.

Subsequently, we repeated this analysis for ground-truth pRF positions falling halfway between neighboring search grid value pairs. In the noise-free case, we simulated time courses for pRFs with 24 different x_0 positions (from -10.625 to +10.625 mm with 49 evenly-spaced values whilst retaining every second value) and 24 different y_0 positions (from -10.625 to +10.625 mm with 49 evenly-spaced values whilst retaining every second value), reflecting 576 locations not matching any search grid value pairs (see Figure 7, lower left panel). In the noise-tainted case, we again selected a subset of these time courses (i.e., the 4th, 8th, 12th, 16th and 20th value out of the 24 x_0 and y_0 positions, respectively), resulting in 25 locations not matching any grid search value pairs (see Figure 9, upper panel). Note that selecting ground-truth pRF positions that coincide with the search grid value pairs should result in 100% accuracy for the noise-free case assuming our pipeline is unbiased. Due to the discretizing nature of grid search fits, an accuracy of 100% is, however, not

achievable for ground-truth pRF positions not matching the search grid value pairs in the noise-free case.

Lastly, just like for the empirical data, we used the simulated odd and even dataset to calculate the median cross-validated goodness-of-fit for all noise-tainted simulations via a 2-fold cross-validation analysis (see 2.7.3 PRF modeling). This allowed us to check that our simulations approximate empirical estimates of median cross-validated goodness-of-fit, indicating that the level of noise we introduced to perturb noise-free time courses was adequate.

Meaningfulness To investigate whether the observed differences in cross-validated goodness-of-fit between the 2dg-fix and the onoff model are meaningful, we simulated a null distribution. To this end, we used the onoff model to simulate a noise-free time series for a pRF with no spatial tuning. We then perturbed this time series 100000 times with random Gaussian noise ($\sigma_{noise} = 2$, expressed in units of mean percent overlap with the pRF model). We did this twice to generate an odd and an even dataset. Just like for the empirical data (see 2.7.3 PRF modeling), we fit both the 2dg-fix model with constrained grid search and the onoff model to the simulated noise-tainted time series of each set and determined the cross-validated goodness-of-fit for each model via a 2-fold cross-validation analysis. We then calculated the difference in cross-validated goodness-of-fit between the 2dg-fix and the onoff model. Using the difference distribution for each cross-validation fold, we determined p-values for a range of small critical difference values (0.01, 0.02, 0.03). To this end, we counted the number of differential values being equal or surpassing our critical value and divided this number by the overall number of differential values. This gives an indication of how probable it is to observe a certain small critical difference if the null hypothesis were true. Finally, just like before, we also determined the median cross-validated goodness-of-fit for both fitted models (see above and 2.7.3 PRF modeling). The entire data analysis pipeline including empirical and simulated data and associated visualizations is publicly available (see Data and code availability). An overview of adopted system environments and software tools can be found in Table S1.

3 Results and interim discussion

3.1 Vibrotactile stimulation produces fingertip clusters in BA3b

Figure 4 shows t-statistic maps reflecting differential brain activity for the contrast stimulation vs baseline (rest) per participant and brain hemisphere. For each participant, we were able to identify a cluster of increased differential brain activity falling entirely into postcentral gyrus and falling entirely into or overlapping right BA3b. These BA3b clusters were small and surrounded by decreases in differential brain activity. Decreases in differential brain activity were also evident for each participant in left BA3b. Overall, this pattern of results is compatible with previous work (Tal et al., 2017) and suggests that we successfully induced responses in right BA3b corresponding to tactile stimulation

of the left fingertip – a prerequisite for pRF modeling.

3.2 Fingertip pRFs in BA3b are larger than the mapping area

Fitting a 2dg model with unconstrained optimization to all runs resulted in pRF parameter estimates (x_0, y_0, σ) in the range of a fraction of a millimeter to 1.59×10^{13} millimeter (i.e., 15900000 km) for the identified BA3b cluster across participants[14]. Extremely large pRF estimates are evidently implausible as no human body could possibly accommodate them. An inspection of the empirically-observed time series suggested that these implausible pRF estimates might be due to broadly-peaked stimulus-evoked responses (for example time courses, see Figure S2-Figure S10). For ordered pRF mapping designs, such as the one adopted here, broad peaks are characteristic of large pRFs, such as pRFs whose size encompasses a large portion of the mapping area or goes well beyond it. Due to the noise being present in empirical time series, broad peaks might be difficult to identify and different broadly-peaked time series difficult to distinguish from one another. This in turn might complicate the unconstrained optimization procedure and result in implausible pRF parameter estimates. To test for this hypothesis, we simulated noise-free and noise-tainted time series for ground-truth pRFs varying in size using a 2dg model and fit a 2dg model with unconstrained optimization to the data.

Figure 5 shows the simulated noise-free time series. This illustration highlights that even without considering the effect of noise, larger pRFs surpassing the mapping area are associated with broader-peaked and less distinctive stimulus-evoked responses. Figure 6 (upper panels) shows the corresponding recovered pRF parameter estimates (x_0, y_0, σ). For all simulated pRF sizes, we were able to closely recover the ground truth. Figure 6 (lower panels) shows the recovered pRF parameter estimates when noise was added to the simulated data. For pRFs within the mapping area, we were able to closely recover the ground truth using the median (apart from for the smallest pRF). However, the larger these pRFs became, the more extreme the percentiles became and thus the range of possible pRF parameter estimates. For pRFs surpassing the mapping area, we were still able to recover the ground truth using the median, albeit less precisely. However, the percentiles of the recovered pRF parameters now indicated an implausibly large range.

Taken together, this pattern of results suggests that for larger pRFs (relative to the mapping area), there is not enough unique information left in a noise-tainted time course to keep the parameter estimates within a plausible range. This does not only lend support to the idea that fingertip pRFs in BA3b are large (relative to the mapping area), but also that we lack the sensitivity to distinguish between different large pRFs, and that an unconstrained optimization procedure with an unlimited parameter space is ill-suited. To address these issues, we therefore constrained the pRF model and fitting procedure. Specifically, we fixed the parameter for pRF size to 8.5 mm, that is, a pRF that basically occupies the whole fingertip, resulting in the 2dg-fix model. We consider such a large pRF

[14] To determine this range, we excluded vertices with a t-value ≤ 0. Considering that manual delineation based on t-statistic maps (see 2.7.1 Functional localization and 3.1 Vibrotactile stimulation produces fingertip clusters in BA3b) is rarely perfectly precise, it can occasionally happen that vertices with t-values ≤ 0 are included in a delineated cluster.

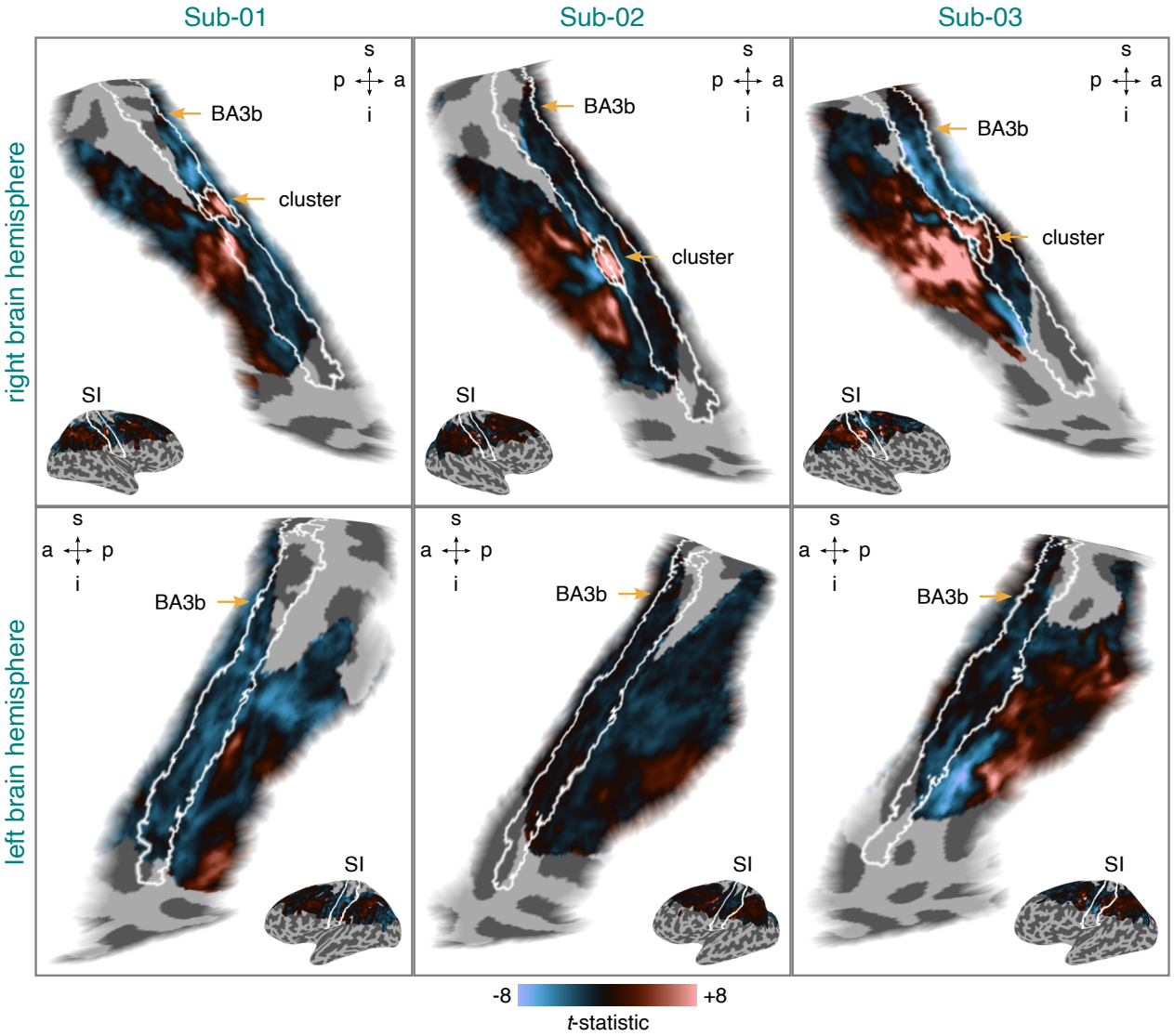

Figure 4. **Differential brain activity for stimulation vs baseline (rest) per participant and brain hemisphere.** The t-statistic maps are based on data from session 1. They were projected onto an inflated cortical surface model where dark gray regions represent sulci and light gray regions gyri. T-statistics surpassing a value of ± 8 were set to this value. BA3b = Brodmann area 3b. SI = primary somatosensory cortex. s = superior. p = posterior. i = inferior. a = anterior. Sub-01, Sub-02, Sub-03 = subject 01, 02, and 03.

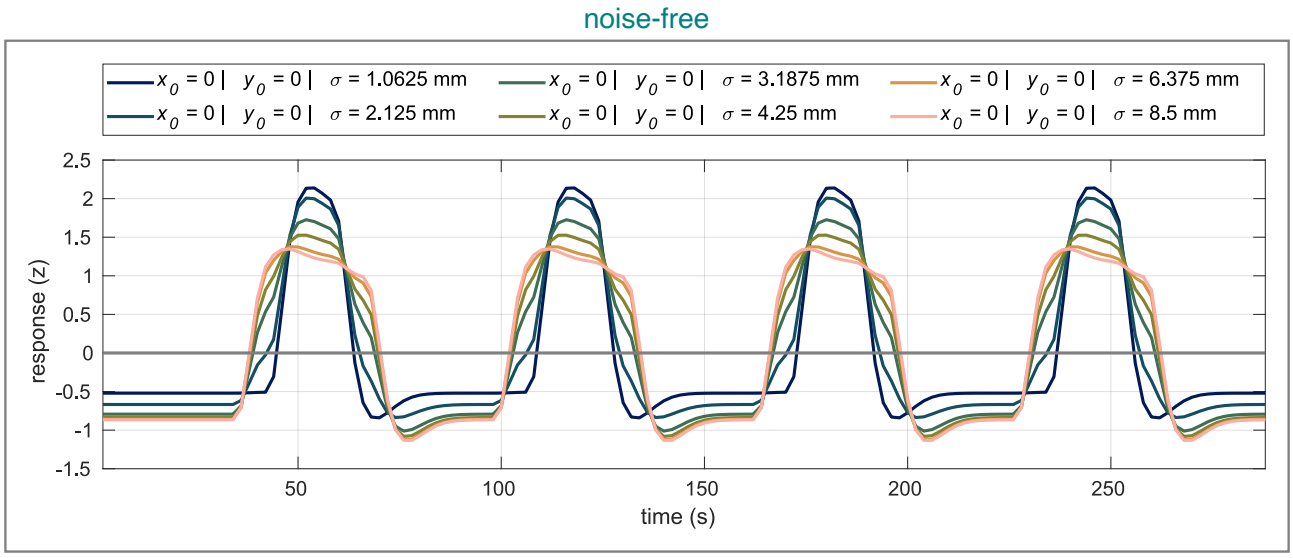

Figure 5. **Noise-free time series simulated using the 2dg model with ground-truth pRFs varying in size.** Legend lists ground-truth pRF parameters. 2dg = 2D Gaussian pRF model. pRF = population receptive field.

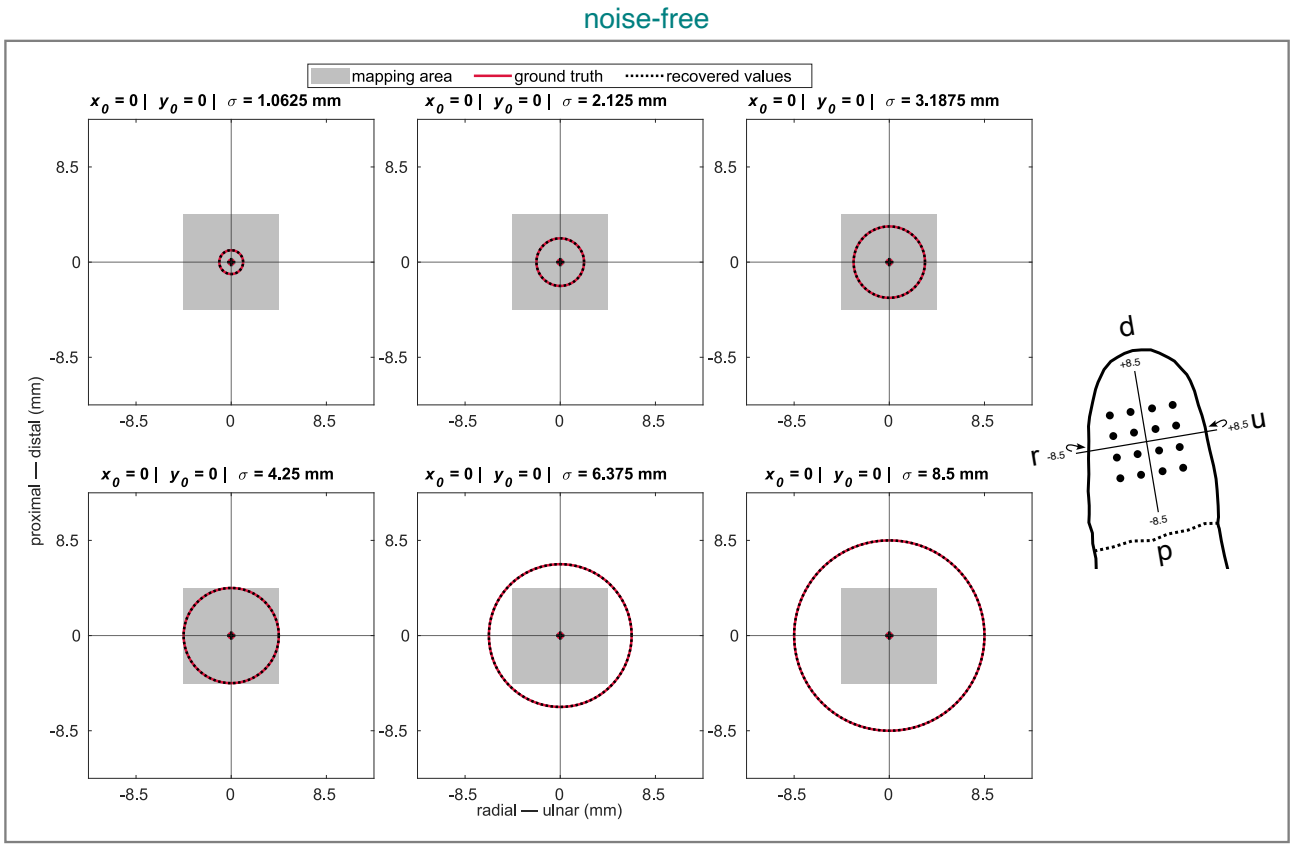

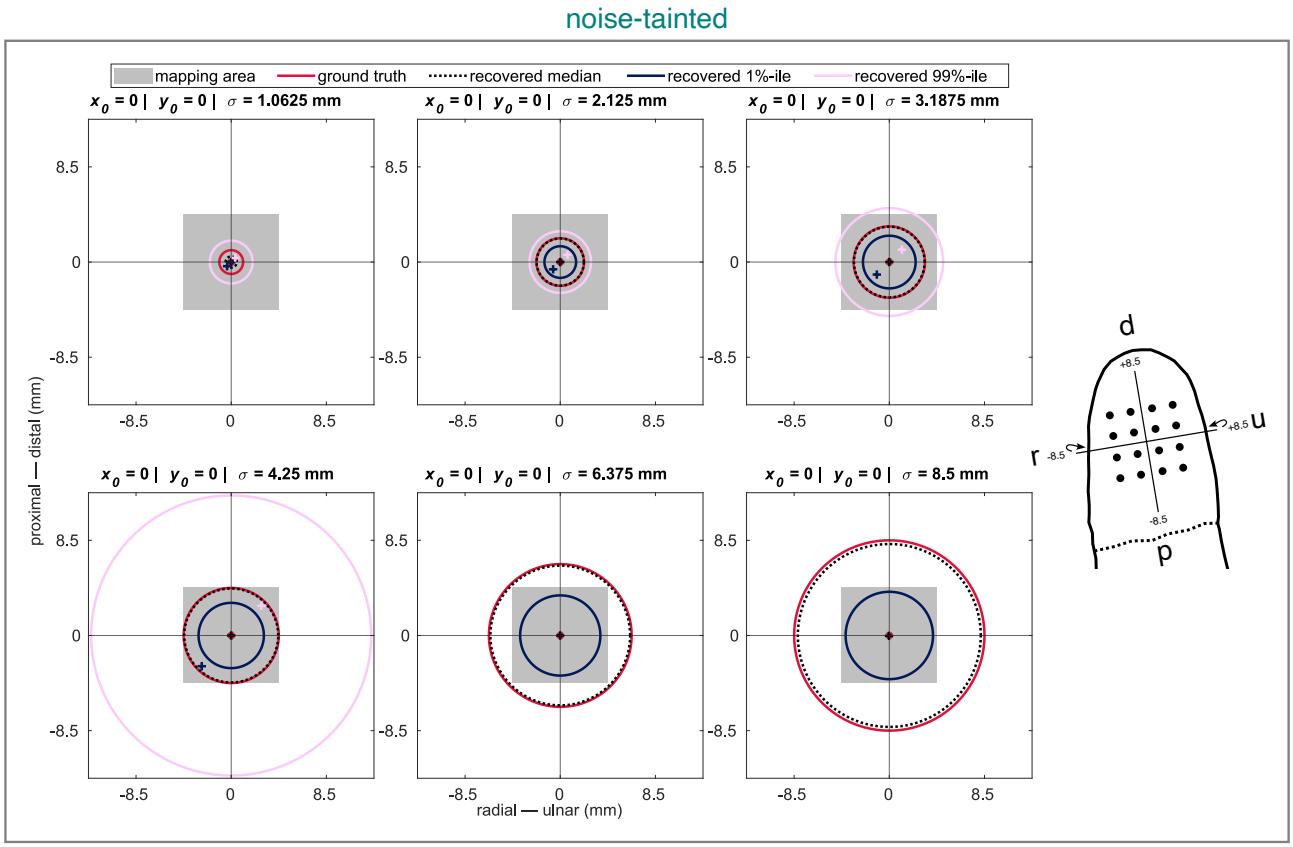

Figure 6. **Recovered pRF estimates for noise-free and noise-tainted time series simulated and fit using the 2dg model with ground-truth pRFs varying in size.** For the noise-tainted time series, 100000 repeats were simulated for each ground-truth pRF. Crosses represent the recovered or ground-truth pRF position. Circles represent the recovered or ground-truth pRF size and are all centered around 0 for better comparison. Note that for the two largest ground-truth pRFs, the lower and upper percentiles for the recovered pRF position estimates and the upper percentile for the recovered pRF size estimate were too large to be displayed. Headers in each panel list ground-truth pRF parameters. %-tile = percentile. 2dg = 2D Gaussian pRF model with unconstrained optimization. pRF = population receptive field. d = distal. p = proximal. r = radial. u = ulnar.

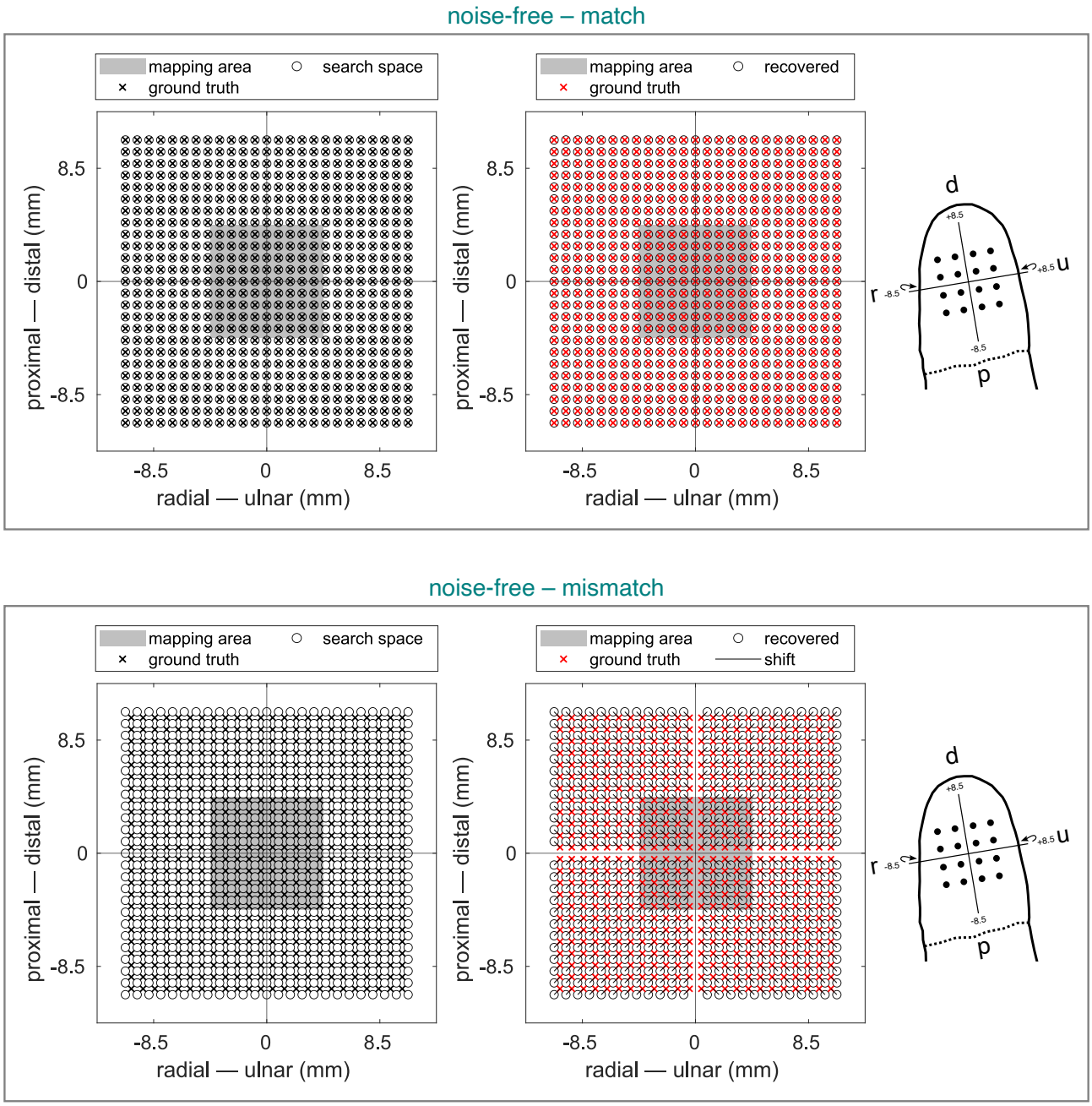

Figure 7. **Recovered pRF position estimates for noise-free time series simulated and fit using the 2dg-fix model with ground-truth pRFs matching or mismatching the search grid value pairs.** Left panels: Ground-truth pRF positions relative to search grid value pairs. Right panels: Ground-truth pRF positions relative to recovered pRF position estimates. 2dg-fix = 2D Gaussian pRF model with parameter for pRF size fixed and constrained grid search. pRF = population receptive field. d = distal. p = proximal. r = radial. u = ulnar.

size reasonable because research in the owl and macaque monkey indicated that receptive fields of neurons in BA3b can occupy almost the entire fingertip (Merzenich et al., 1978; Nelson et al., 1980; Sur et al., 1980)[15]. In addition to that, we used the constrained grid search fits that are based on a limited parameter space as final pRF estimates. Before applying this refined procedure to our empirical data, though, we performed a series of simulations to investigate its computational validity (accuracy).

[15]Importantly, however, the receptive fields measured in these studies were minimum receptive fields, defined as the area on the skin where light tactile stimulation evoked a maximal response.

3.3 PRF estimates are computationally accurate within limits

Figure 7 (upper panels) shows the recovered pRF parameters (x_0, y_0) for ground-truth pRFs varying in position and coinciding with the search grid value pairs when no noise was added to the simulated data. The simulated data were obtained using the 2dg-fix model and the model fits via the 2dg-fix model with constrained grid search. For all simulated pRF positions, we were able to recover the ground truth with an accuracy of 100%. Figure 8 shows the frequency of recovered pRF parameters for the same scenario when noise was added to the simulated data, albeit only for a subset of ground-truth pRF positions. For almost all simulated pRF positions, the most frequently recovered pRF parameters were solely located in close vicinity of the ground truth. For simulated pRF positions close to the boundary of the search space, however, the most frequently recovered pRF parameters were additionally located at the very edge of the search space. Such edge artifacts are expected due to the limits of the search space. Importantly, for all simulated pRF positions, the less frequently recovered pRF parameters were considerably scattered around the ground truth.

To assess the generality of these results, we repeated the simulation analysis for ground-truth pRFs whose position did not coincide with the search grid value pairs. Figure 7 (lower panels) shows the recovered pRF parameters (x_0, y_0) for the noise-free case and Figure 9 for the noise-tainted case. Whereas the noise-tainted case largely mirrored our previous observations, the noise-free case additionally illustrated that for all simulated pRF positions, the recovered pRF parameters are systematically biased, albeit still very close to the ground truth. Such biases are expected due to the discretized nature of the search space.

Taken together, these results illustrate that under conditions of no noise, our pRF estimates are computationally accurate, but might suffer from small systematic biases induced by the discretization of the search space. Under conditions of noise, the computational accuracy is further compromised by edge artifacts and a non-negligible spatial uncertainty of parameter estimates. It is important to keep these aspects in mind when interpreting any empirical pRF position gradients.

3.4 Fingertip pRFs are organized so that the ulnar-to-radial axis along the fingertip maps onto an inferior-to-posterior axis in BA3b

Figure 10 shows the pRF position estimates (x_0, y_0) for the identified BA3b cluster per participant and dataset. The pRF position estimates were obtained using the 2dg-fix model with constrained grid search. The corresponding pRF baseline (β_0) and pRF amplitude (β_1) parameters are displayed in Figure S11. The x_0 position estimates based on all runs indicated that the ulnar-to-radial axis spanning the fingertip maps onto a superior-to-inferior axis in BA3b for both Sub-01 and Sub-02. For Sub-03, however, such a gradient was not clearly visible. A split-half analysis showed that the quantified x_0 map for Sub-01 and Sub-02 was largely reliable across odd and even runs. For Sub-03, however, this analysis flagged that the more inferior part of the x_0 map was rather unreliable.

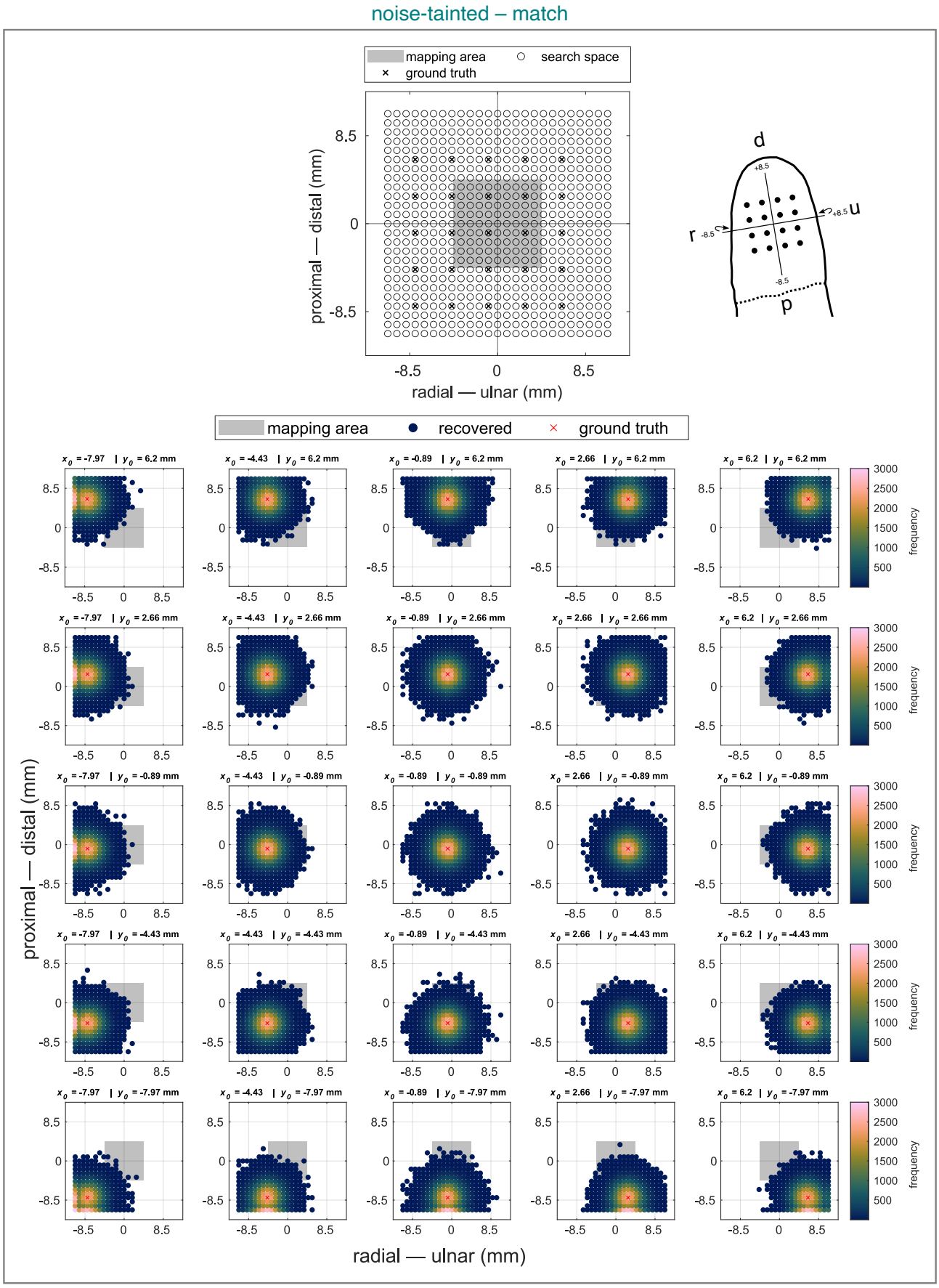

Figure 8. **Recovered pRF position estimates for noise-tainted time series simulated and fit using the 2dg-fix model with ground-truth pRFs matching the search grid value pairs.** Upper panel: Ground-truth pRF positions relative to search grid value pairs. Lower panel: Ground-truth pRF positions relative to recovered pRF position estimates. For each ground-truth pRF, 100000 repeats were simulated and the number of times a certain grid search value pair was recovered was counted. Note that although we simulated an odd and and even dataset (see text for details), for reasons of brevity, we only present the results of the even dataset here. Headers in smaller panels list ground-truth pRF parameters. 2dg-fix = 2D Gaussian pRF model with parameter for pRF size fixed and constrained grid search. pRF = population receptive field. d = distal. p = proximal. r = radial. u = ulnar.

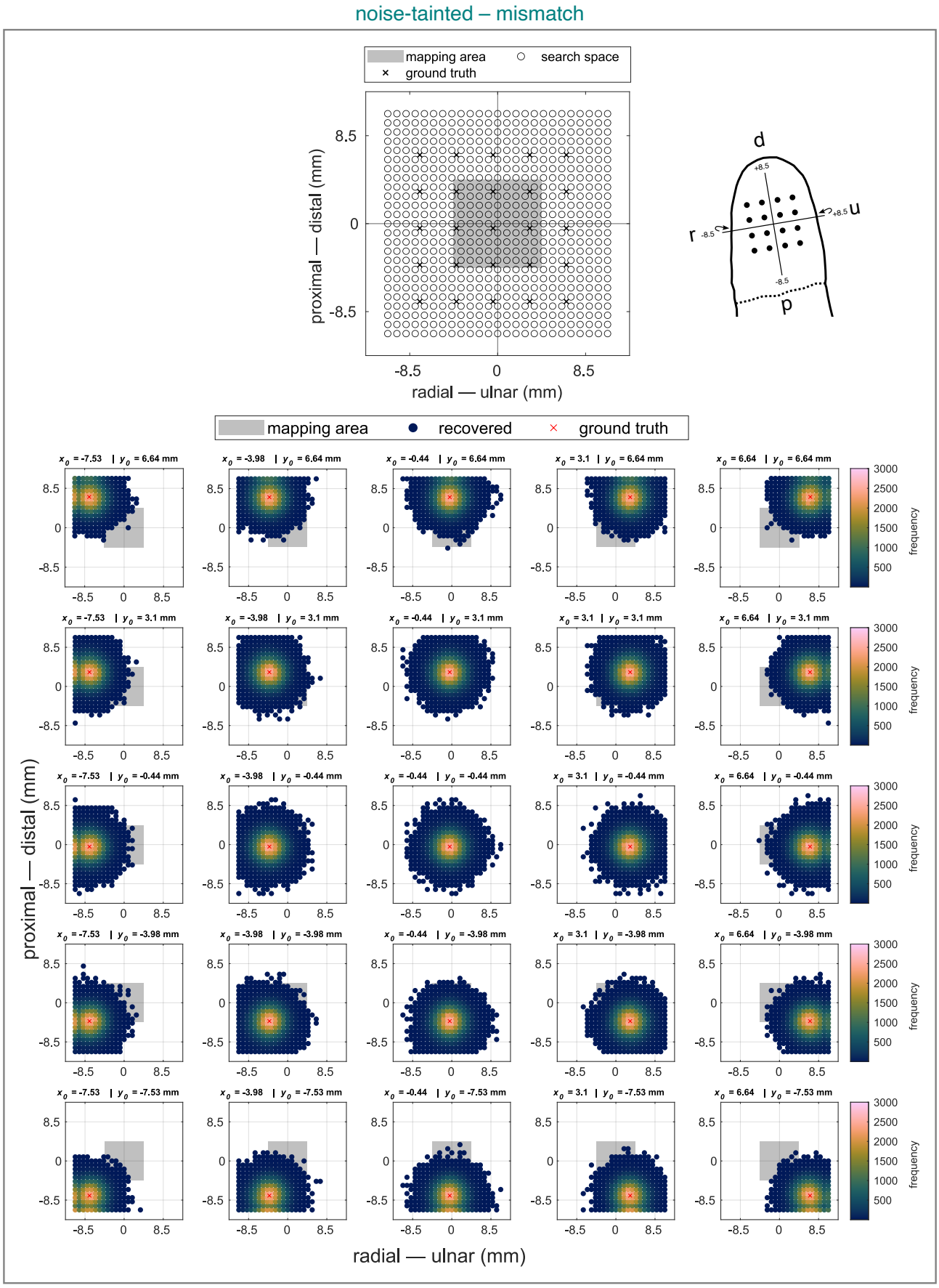

Figure 9. **Recovered pRF positions estimates for noise-tainted time series simulated and fit using the 2dg-fix model with ground-truth pRFs mismatching the search grid value pairs.** Upper panel: Ground-truth pRF positions relative to search grid value pairs. Lower panel: Ground-truth pRF positions relative to recovered pRF position estimates. For each ground-truth pRF, 100000 repeats were simulated and the number of times a certain grid search value pair was recovered was counted. Note that although we simulated an odd and and even dataset (see text for details), for reasons of brevity, we only present the results of the even dataset here. Headers in smaller panels list ground-truth pRF parameters. 2dg-fix = 2D Gaussian pRF model with parameter for pRF size fixed and constrained grid search. pRF = population receptive field. d = distal. p = proximal. r = radial. u = ulnar.

For the y_0 position estimates based on all runs, no clear position gradient was evident across participants with a plethora of estimates being positive and large in magnitude. Nonetheless, just like for the x_0 position estimates, a split-half analysis suggested that the quantified y_0 maps for Sub-01 and Sub-02 were largely reliable across odd and even runs, whereas the inferior part of the y_0 map was rather unreliable for Sub-03.

In sum, our results speak to a fine-grained somatotopic x_0 position gradient corresponding to the fingertip in BA3b. However, in light of the unclear y_0 position gradient and the imposed modeling constraints, the question arises as to whether we indeed found evidence for spatially-tuned pRFs. To address this question, we next investigated to what extent the 2dg-fix model has superior explanatory power over a model without any spatial tuning (onoff model).

3.5 Fingertip pRFs in BA3b are spatially-tuned

Figure 11 shows the cross-validated goodness-of-fit (cR^2) for the 2dg-fix model and the onoff model or the difference thereof (*diff*-cR^2) for the identified BA3b cluster per participant and cross-validation fold. Overall, the cross-validated goodness-of-fit for both models was decent for all participants. Moreover, consistent with the split-half analysis for the pRF position estimates, cross-validated goodness-of-fit for the inferior part of Sub-03's position map was rather low. Importantly, these tendencies appeared to be largely consistent across cross-validation folds. When contrasting the cross-validated goodness-of-fit for the 2dg-fix model to the onoff model directly, the 2dg-fix model slightly outperformed the onoff model in various locations for all participants, which was largely consistent across both cross-validation folds. Specifically, across vertices, participants, and cross-validation folds, the difference in cross-validated goodness-of-fit in favor of the 2dg-fix model ranged from just slightly above 0 to 0.1488[16] (14.88%; for example time courses, see Figure S2-Figure S10). To investigate whether differences of this magnitude are meaningful and we thus indeed found evidence for spatially-tuned pRFs, we additionally simulated a null distribution.

Figure 12 shows the simulated differences in cross-validated goodness-of-fit (*diff*-cR^2) for the 2dg-fix vs the onoff model when noise was added to the simulated data per cross-validation fold. The simulated data were obtained using the onoff model. The model fits were obtained using the onoff model and the 2dg-fix model with constrained grid search. The difference distribution was clearly negatively skewed. Moreover, the p-values calculated for a range of critical differences suggested that even slight differences in favor of the 2dg model are unlikely to be observed by chance and might

[16] To determine this range, we excluded vertices with a t-value ≤ 0 and vertices for which at least one of the pRF models (2dg-fix or onoff) exhibited a negative cross-validated goodness-of-fit. The latter was done separately for each cross-validation fold. Considering that manual delineation based on t-statistic maps (see 2.7.1 Functional localization and 3.1 Vibrotactile stimulation produces fingertip clusters in BA3b) is rarely perfectly precise, it can occasionally happen that vertices with t-values ≤ 0 are included in a delineated cluster. Similarly, unlike traditional quantifications of goodness-of-fit using a single dataset, the cross-validated quantification adopted here can occasionally result in negative cross-validated goodness-of-fit values. Although these negative values are expected, they cannot be readily interpreted in the scope of the present modeling framework and were thus excluded.

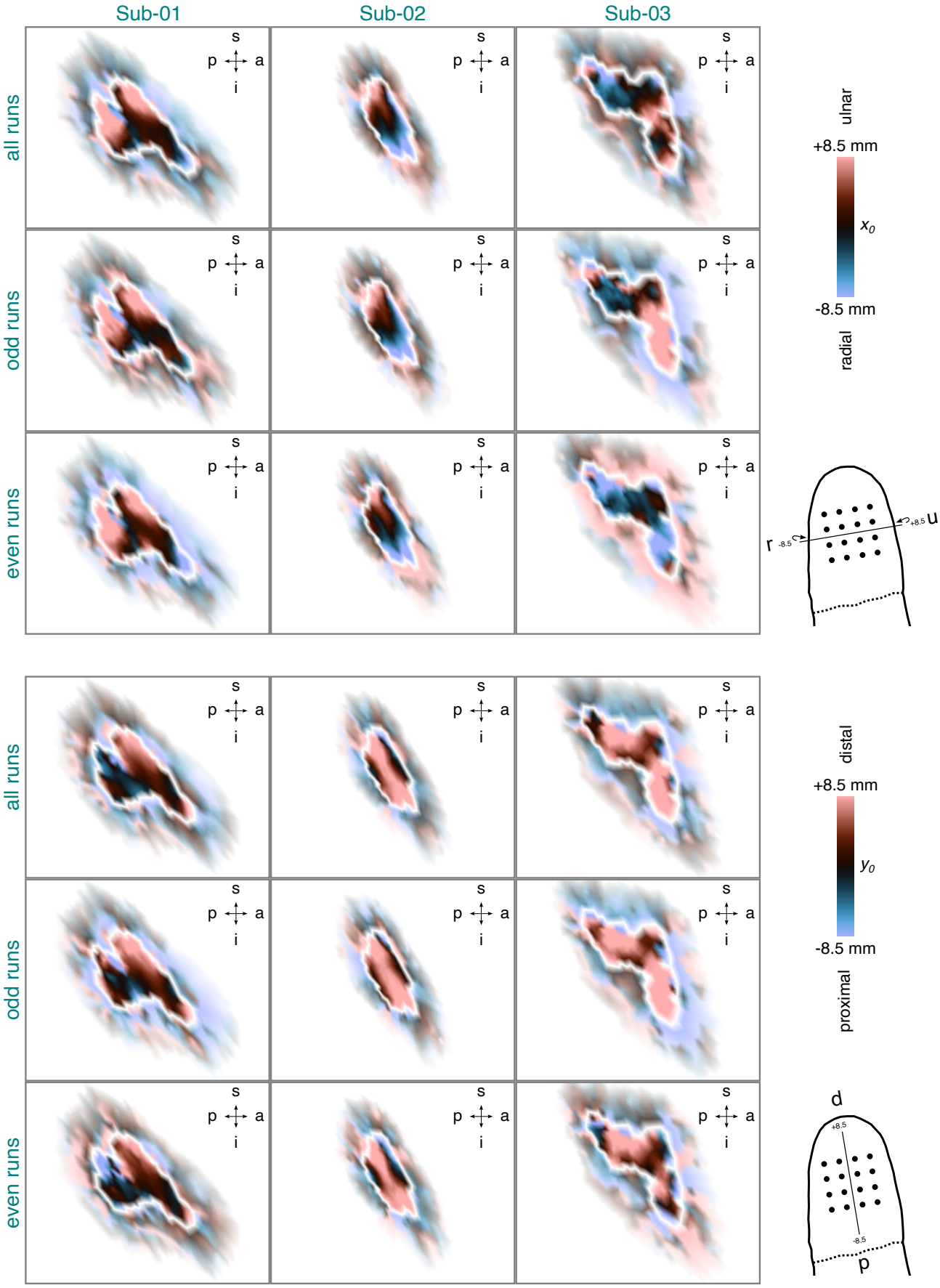

Figure 10. **PRF position estimates for the identified BA3b cluster and the 2dg-fix model per participant and dataset.** The x_0 and y_0 estimates are based on data from session 2-4. They were projected onto an inflated cortical surface model where dark gray regions represent sulci and light gray regions gyri. A zoomed-in view is shown here. Any x_0 and y_0 estimates surpassing a value of ± 8.5 mm were set to this value. White lines denote the extent of the identified BA3b cluster (see Figure 4). BA3b = Brodmann area 3b. s = superior. p = posterior. i = inferior. a = anterior. Sub-01, Sub-02, Sub-03 = subject 01, 02, and 03. 2dg-fix = 2D Gaussian pRF model with parameter for pRF size fixed and constrained grid search. pRF = population receptive field. d = distal. p = proximal. r = radial. u = ulnar.

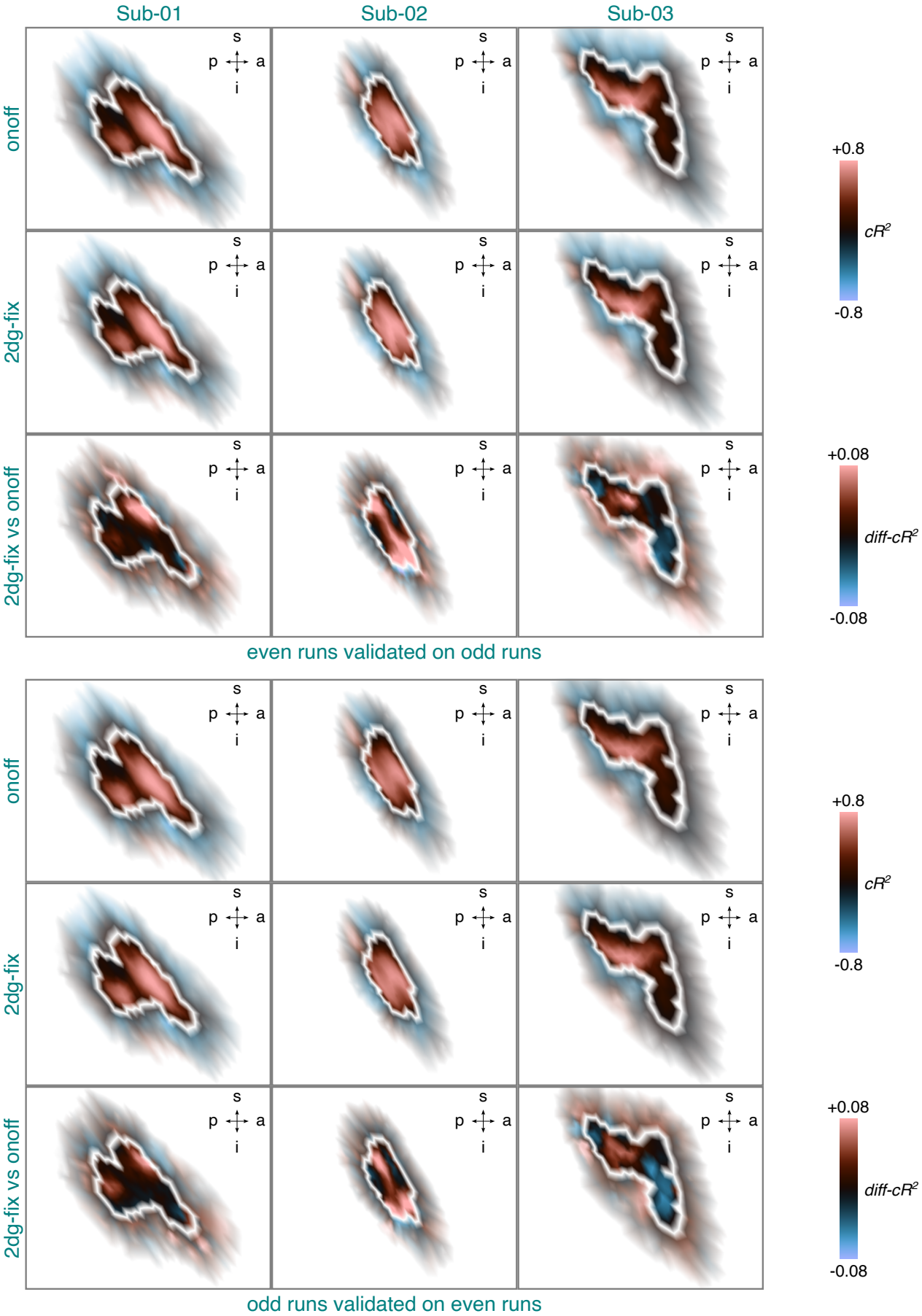

Figure 11. **Cross-validated goodness-of-fit for the 2dg-fix and the onoff model or the difference thereof for the identified BA3b cluster per participant and cross-validation fold.** The cR^2 or diff-cR^2 values are based on data from session 2-4. They were projected onto an inflated cortical surface model where dark gray regions represent sulci and light gray regions gyri. A zoomed-in view is shown here. Any cR^2 or diff-cR^2 values surpassing a value of ± 0.8 or ± 0.08 were set to this value, respectively. White lines denote the extent of the identified BA3b cluster (see Figure 4). BA3b = Brodmann area 3b. s = superior. p = posterior. i = inferior. a = anterior. Sub-01, Sub-02, Sub-03 = subject 01, 02, and 03. 2dg-fix = 2D Gaussian pRF model with parameter for pRF size fixed and constrained grid search. onoff = pRF model without any spatial tuning that simply reflects the presence or absence of tactile stimulation. pRF = population receptive field. *diff-*cR^2 = differential cR^2.

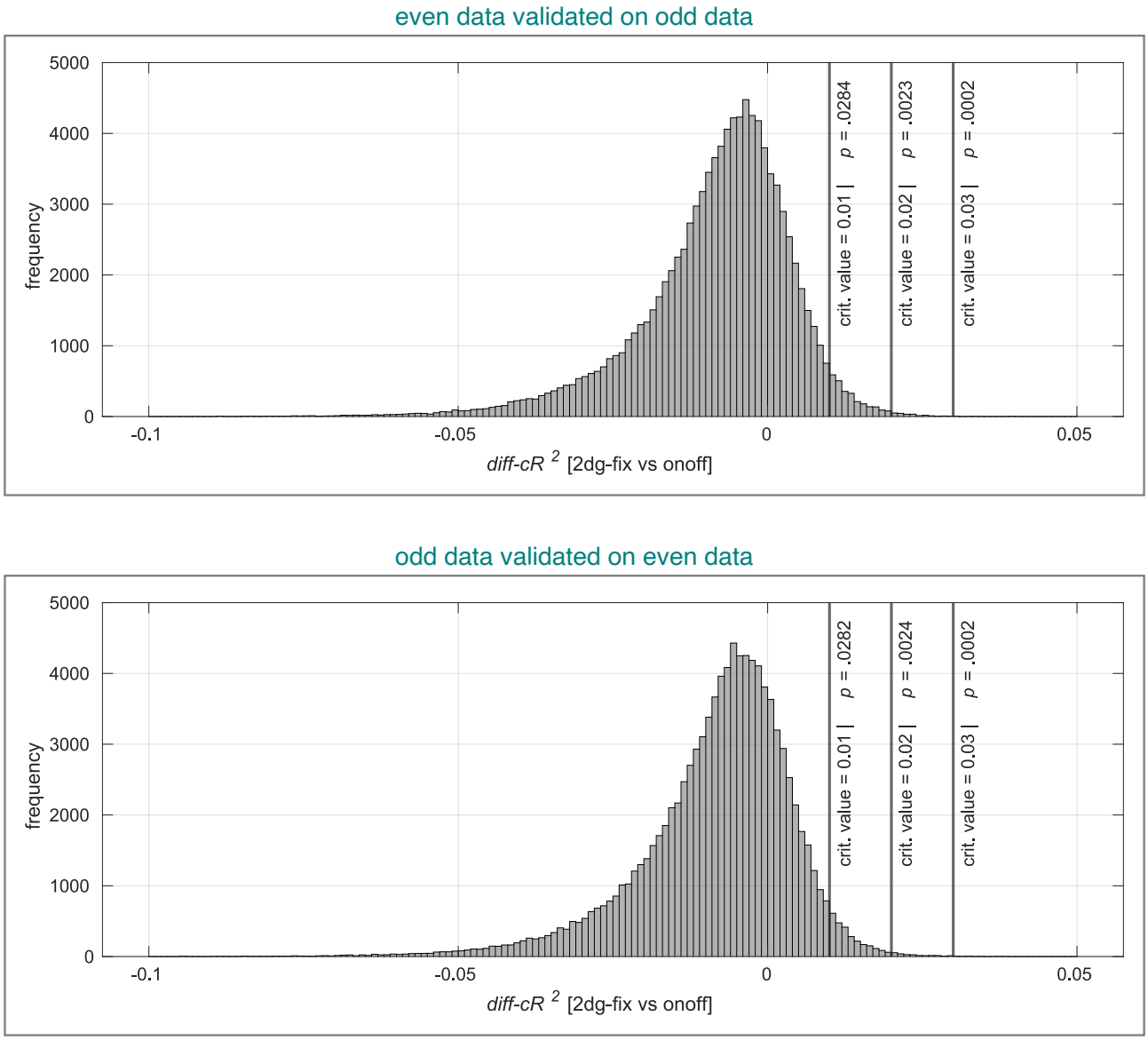

Figure 12. **Simulated difference in cross-validated goodness-of-fit for the 2dg-fix vs the onoff model per cross-validation fold.** Noise-tainted time series were simulated using the onoff model with 100000 repeats for each cross-validation fold and both the 2dg-fix and the onoff model were fit to the simulated data. Histogram bins ranged from -0.1 to +0.05 with a constant bin width of 0.001. 2dg-fix = 2D Gaussian pRF model with parameter for pRF size fixed and constrained grid search. onoff = pRF model without any spatial tuning that simply reflects the presence or absence of tactile stimulation. pRF = population receptive field. crit. = critical. *diff-*cR^2 = differential cR^2.

thus be meaningful. Both these tendencies were consistent across cross-validation folds. Overall, these results not only indicate that we found evidence for spatially-tuned pRFs, but also that the x_0 position gradient we identified appears to be meaningful.

However, any claims about the meaningfulness of observed difference in cross-validated goodness-of-fit require that the simulated null distribution and thus the level of noise we used to perturb noise-free time series was adequate. The same is true for any claims about the computational validity of our pRF estimates. To address these issues, we next investigated to what extent the overall explanatory power, that is, the median cross-validated goodness-of-fit, differs between empirical and simulated data. In doing so, we also investigated to what extent the overall explanatory power varies between participants and fitted models.

3.6 Empirical overall explanatory power is variable and similar to simulated one

Table S2 shows the median cross-validated goodness-of-fit (cR^2) for each participant or simulation type as a function of fitted pRF model and cross-validation fold. Whereas the median cross-validated goodness-of-fit varied slightly between cross-validation folds for each participant and fitted pRF model, the variability across participants was much greater, with Sub-02 showing the highest median values, followed by Sub-01 and then by Sub-03. These interindividual differences resonate well with both the split-half analysis for pRF position estimates and prior analyses involving cross-validated goodness-of-fit and suggest that the overall explanatory power was highest for Sub-02. This increase not only needs to be considered when interpreting empirical pRF position gradients, but also provided an upper benchmark for evaluating the appropriateness of our simulations. Considering that the median cross-validated goodness-of-fit for all simulations lay well within the range observed for Sub-02, the overall explanatory power was comparable in this case. As such, the level of noise we used to perturb noise-free time courses can be considered adequate.

Apart from these observations, it is worth noting that for all participants except Sub-03, the median cross-validated goodness-of-fit tended to be higher for the fitted 2dg-fix model as compared to the fitted onoff model across both cross-validation folds. Notably, this difference in median cross-validated goodness-of-fit between the fitted models was absent for both cross-validation folds when we simulated data using the onoff model. These findings mirror our previous results for empirical and simulated differences in cross-validated goodness-of-fit, broadly corroborating the idea that we found evidence for spatially-tuned tactile pRFs.

4 General discussion

In the present study, we sought to estimate fine-grained 2D spatio-tactile pRFs of the tip of the index finger for the first time in human SI. To this end, we recorded brain responses whilst finely stimulating a portion of participants' fingertips vibro-tactilely and focused on BA3b as a region of interest. As a first step, we fit a 2D Gaussian pRF model to the data using an unconstrained fitting procedure. This resulted in implausible estimates for pRF position and size, suggesting the recorded brain responses do not contain enough unique information to keep the estimates within a plausible range. Simulations indicated that this likely occurred because the size of pRFs in BA3b exceeds the mapping area on the fingertip skin, resulting in partial pRF mapping and thus less distinct brain responses. As a second step, we therefore constrained the fitting procedure and the 2D Gaussian pRF model by fixing pRF size. When doing so, our results for pRF position indicated that the ulnar-to-radial axis along the fingertip is represented along a superior-to-inferior axis in BA3b, whilst no clear pRF position gradient was discernible for the distal-to-proximal-axis. Although this pattern of results was largely consistent within and across participants (2 out of 3), a cross-validated model

comparison showed that our constrained 2D Gaussian pRF model only slightly outperforms a pRF model without any spatial tuning in various cortical locations. However, simulations highlighted that even such slight differences might be meaningful and with that the pRF position estimates we obtained. Collectively, these findings shed first light onto the fine-grained functional architecture of human fingertip maps.

4.1 The size of fingertip pRFs in BA3b

Our finding of putatively large fingertip pRFs (relative to the mapping area) in human BA3b appears compatible with invasive recordings in the owl and macaque monkey showing that the area of excitatory receptive fields in BA3b can range from a subportion of to almost the entire fingertip (Merzenich et al., 1978; Nelson et al., 1980; Sur et al., 1980). Although we cannot make any firm statements about the exact size of fingertip pRFs in human BA3b, our simulations suggest that for a pRF sitting at the middle of the mapping area, pRF size is likely larger than the mapping area, and thus 4.25 mm. Such large pRFs can arise from a multitude of neuronal and non-neuronal sources.

4.1.1 Neuronal sources

As far as neuronal sources are concerned, it is important to appreciate that large fingertip pRFs can result from both small receptive fields of single BA3b neurons with a large position scatter or truly large receptive fields with a small position scatter. Similarly, they can arise from only a few large receptive fields of single BA3b neurons biasing the population estimate. Without having an estimate of the variance of receptive field properties within a voxel in BA3b and modeling this aspect explicitly, it is impossible to distinguish between these possibilities.

Leaving these ambiguities aside, it is conceivable that large fingertip pRFs reflect the existence of receptive fields elongated along the distal-to-proximal axis of the finger. In line with this, invasive recordings in owl and macaque monkeys show that the shape of receptive fields in BA3b can range from circular to elliptical (Merzenich et al., 1978; Nelson et al., 1980; Sur et al., 1980). As such, expanding the mapping area along the distal-to-proximal axis of the finger might be critical for obtaining a direct estimate of the size and eventually also the shape of fingertip pRFs.

Similarly, it is possible that large fingertip pRFs evince the existence of multi-digit receptive fields. In fact, electrophysiological studies in macaque monkeys suggest that a subportion of BA3b neurons responds to tactile stimulation to multiple fingers (DiCarlo et al., 1998; Lazar et al., 2022; Trzcinski et al., 2023). Human fMRI studies modeling pRFs along the between-fingertip dimension also show tendencies for multi-digit pRFs, although it is not always clear whether these are indeed present in BA3b (P. Liu et al., 2021; Puckett et al., 2020; Schellekens et al., 2021). Importantly, these considerations suggest that it might be necessary to expand the mapping area to other fingers to obtain comprehensive estimates of the size as well as shape of fingertip pRFs.

Lastly, large fingertip pRFs might be related to the type of stimulation we applied. Specifically, we adopted a position-changing vibrotactile stimulus consisting of a row of pins that oscillated at a frequency of 25 Hz with brief on and off periods. This stimulus might have not only been effective in driving Merkel cell neurite complexes and Meissner corpuscles, mechanoreceptors known to have small peripheral receptive fields (area: $\sim$9 mm^2 and $\sim$22 mm^2, respectively), but also Pacinian corpuscles, mechanoreceptors known to have large peripheral receptive fields (e.g., entire finger; as summarized in Johnson, 2002). This is because all these mechanoreceptors are known to be sensitive to a range of frequencies including 25 Hz (Merkel: $\sim$0-100 Hz; Meissner: $\sim$1-300 Hz; Pacinian: $\sim$5-1000 Hz), albeit their peak sensitivities are thought to differ markedly (Merkel: $\sim$5 Hz; Meissner: $\sim$50 Hz; Pacinian: $\sim$200 Hz; as summarized in Johnson, 2002). What is more, locally applied vibrotactile stimulation is known to result in surface waves propagating through the skin, effectively enlarging the stimulus and limiting its resolution (Dandu et al., 2021; Manfredi et al., 2012; Sofia & Jones, 2013; Tummala et al., 2024). Depending on how pronounced and far-reaching these propagating waves were, they might have led to a fairly effective stimulation of the large peripheral receptive fields of Pacinian corpuscles despite our small mapping area, which might have manifested itself at the cortical level too.

4.1.2 Non-neuronal sources

As far as non-neuronal sources are concerned, it may be argued that large pRF sizes are due to the brain's macrovasculature. This is because fMRI measures a hemodynamic response (Logothetis, 2003) and BOLD fMRI, as applied in our study, is known to be sensitive to large draining veins, such as those near the pial surface (Bause et al., 2020; Koopmans et al., 2010; Polimeni et al., 2010). This sensitivity might lead to a systematic blurring of fMRI time series near the pial surface and thus an inflation of pRF size estimates. It is important to note, however, that our analyses were limited to voxels located midway between vertices on the gray-white matter and pial boundary. Moreover, pRF size estimates in human visual cortex based on BOLD-fMRI have been shown to vary according to a u-shaped function across cortical depth (Fracasso et al., 2016). And lastly, visual pRF mapping in macaque monkeys shows that BOLD-fMRI-based pRF size estimates and variations thereof closely reflect those obtained via direct neural recordings (Klink et al., 2021). As such, our finding of putatively large pRF sizes (relative to the mapping area) cannot be easily dismissed as a mere effect of the brain's macrovasculature.

Another factor that may have led to a blurring of the fMRI time series and thus an inflation of pRF size estimates is body motion, such as movements of the head or hand. However, the effect of body motion on fMRI time series is likely complex, depending, amongst other things, on the nature and location of movement, how body movements interact with the image acquisition process (e.g., T. T. Liu, 2017; Zaitsev et al., 2015), and how and if cutaneous, proprioceptive, and motor information is integrated in BA3b (e.g., Kim et al., 2015). As such, a one-to-one relationship between an increase in body motion and an increase in pRF size seems unlikely. Moreover, it is

important to consider that 2 of our 3 participants were highly experienced fMRI participants and all participants familiarized themselves with the pRF mapping experiment prior to scanning, had their hand stabilized using a cushion, and were explicitly instructed to keep still. In addition, our data were prospectively corrected for within-run head motion and retrospectively for between-run head motion via a carefully designed procedure. As such, it seems unlikely that hand or head motion was a primary driving factor.

4.2 The organization of fingertip pRFs in BA3b

Our finding of a pRF position gradient where the ulnar-to-radial axis along the fingertip maps onto a superior-to-inferior axis in BA3b fits in with invasive recordings in the owl and macaque monkey showing a similar topographic organization (Merzenich et al., 1978; Nelson et al., 1980). However, unlike these invasive recordings, our findings revealed no clear pRF position gradient for the distal-to-proximal axis along the finger(tip) in BA3b. Similar to our incapacity to obtain a direct estimate of pRF size, this might be due to large receptive fields that are elongated along the distal-to-proximal axis (Merzenich et al., 1978; Nelson et al., 1980; Sur et al., 1980) and a mapping area that was too small to account for this.

Importantly, the pRF position gradient we uncovered for the ulnar-to-radial axis was not discernible for 1 out of our 3 participants. Given that the inferior part of both pRF position maps was rather unreliable for this participant and characterized by a low cross-validated goodness-of-fit, this inter-individual variability seems, at least partly, due to an increased level of noise for this participant. Importantly, however, invasive recordings in owl and squirrel monkeys point to considerable inter-individual variability in the architecture of hand maps in BA3b (Merzenich et al., 1987). It is therefore vital to assess the test-retest reliability as well as cross-validated goodness-of-fit within a given participant and across participants to distinguish intra- from inter-individual variation in pRF properties, as we did here.

4.3 Study limitations

PRF modeling is only as sensible as the data and assumptions it operates upon. To collect high-quality datasets, we combined 7T-fMRI at submillimeter resolution, precision neuroscience, PMC, and fine-grained vibrotactile stimulation. Despite this effort, our findings suggest that the usefulness of these datasets is limited because of partial pRF mapping. Future studies aimed at resolving fine-grained 2D spatio-tactile pRFs should therefore try to map out body parts as completely as possible whilst ensuring a dense sampling of the skin. Yet, due to the general lack of commercially-available high-density tactile stimulation equipment that is MRI-compatible, this is a challenging endeavor.

Besides, both the explanatory power and computational accuracy of our pRF estimates may be limited by the assumptions we made about the HRF in BA3b. Given that we adopted a canonical HRF, we assumed invariance across voxels(vertices) and individuals, which is not necessarily the

case. However, accurately estimating voxel-wise(vertex-wise) HRF parameters in individual brains is challenging and susceptible to noise, thus requiring a large amount of additional data.

The explanatory power and computational accuracy may be furthermore compromised by the assumptions we made about the resolution and extent of tactile stimulation. More precisely, although vibrotactile stimulation is known to result in surface waves propagating through the skin (Dandu et al., 2021; Manfredi et al., 2012; Sofia & Jones, 2013; Tummala et al., 2024), the way we represented the tactile stimulus as part of our pRF modeling pipeline does not account for this. Before any such incorporation can happen, though, it is necessary to quantify the properties of propagating waves for a given pRF mapping design via suitable techniques, such as vibrometry (Dandu et al., 2021; Manfredi et al., 2012; Tummala et al., 2024).

Lastly, the adequateness of our simulations might be limited by the assumptions we made about the noise. Specifically, we assumed additive white Gaussian noise across voxels(vertices). As such, we did, for instance, not account for potential noise correlations between neighboring voxels(vertices), potential differences in the level of noise across voxels(vertices), or different sources of noise (e.g., T. T. Liu, 2017; Welvaert & Rosseel, 2014; Zhang et al., 2020). Pitting different noise models against one another is beyond the scope of the present article, but represents an important avenue for future research.

5 Summary and conclusion

Despite the great importance of fingertip sensations for everyday life, little is known about how tactile input to the fingertips is represented in human SI. Using 2D spatio-tactile pRF modeling, we show – for the first time – that fingertip pRFs in human BA3b may be large (relative to the mapping area) and organized so that the ulnar-to-radial axis across the fingertip maps onto a superior-to-inferior axis in human BA3b. Although we were unable to obtain a direct estimate of pRF size and a clear pRF position gradient for the distal-to-proximal axis along the fingertip, our results bring us closer to understanding the fine-grained architecture of fingertip maps in the human brain.

Data and code availability

Data and materials including custom code associated with this manuscript are available via our OSF, OpenNeuro, and GitHub repositories.

Contributions

SS: Conceptualization, Methodology, Software, Validation, Formal analysis, Investigation, Data curation, Writing – Original Draft, Writing – Review & Editing, Visualization, Project administration.

FL: Methodology, Software, Validation, Formal analysis, Investigation, Data curation, Writing – Review & Editing. DSS: Conceptualization, Methodology, Software, Validation, Data curation, Writing – Review & Editing. HM: Methodology, Investigation, Writing – Review & Editing. PL: Investigation, Writing – Review & Editing. JN: Investigation, Writing – Review & Editing. EK: Conceptualization, Resources, Writing – Review & Editing, Supervision, Project administration, Funding acquisition.

Declaration of competing interests

The authors declare no competing interests.

Acknowledgments

The present work received funding from the European Structure and Investment Fund (ZS/2020/05/141591), the European Research Council under the European Union's Horizon 2020 research and innovation programme (949609) as well as the Deutsche Forschungsgemeinschaft (MA, 9235/3-1, 501214112 and KU 3711/4-1, 528318902). We thank Astrid Wollrab and Cindy Lübeck for help with data collection, Juliane Döhler for discussions about the quality of our segmentation results, Udo Adler for computing support, and the University Clinic for Oral and Maxillofacial Surgery in Magdeburg for manufacturing high-quality mouthpieces.

References

Alvarez, I., de Haas, B., Clark, C. A., Rees, G., & Schwarzkopf, D. S. (2015). Comparing different stimulus configurations for population receptive field mapping in human fMRI. *Frontiers in Human Neuroscience*, *9*, 96. https://doi.org/10.3389/fnhum.2015.00096

Ashburner, J., & Friston, K. J. (2005). Unified segmentation. *NeuroImage*, *26*, 839–851. https://doi.org/10.1016/j.neuroimage.2005.02.018

Bause, J., Polimeni, J. R., Stelzer, J., In, M.-H., Ehses, P., Kraemer-Fernandez, P., Aghaeifar, A., Lacosse, E., Pohmann, R., & Scheffler, K. (2020). Impact of prospective motion correction, distortion correction methods and large vein bias on the spatial accuracy of cortical laminar fMRI at 9.4 Tesla. *NeuroImage*, *208*, 116434. https://doi.org/10.1016/j.neuroimage.2019.116434

Blankenburg, F., Ruben, J., Meyer, R., Schwiemann, J., & Villringer, A. (2003). Evidence for a rostral-to-caudal somatotopic organization in human primary somatosensory cortex with mirror-reversal in areas 3b and 1. *Cerebral Cortex*, *13*, 987–993. https://doi.org/10.1093/cercor/13.9.987

Boré, A., Guay, S., Bedetti, C., Meisler, S., & Guenther, N. (2021). Dcm2bids (version 2.1.6). https://github.com/UNFmontreal/Dcm2Bids

Brainard, D. H. (1997). The Psychophysics Toolbox. *Spatial Vision*, *10*, 433–436. https://doi.org/10.1163/156856897X00357

Choi, M.-H., Kim, S.-P., Kim, H.-S., & Chung, S.-C. (2016). Inter-and intradigit somatotopic map of high-frequency vibration stimulations in human primary somatosensory cortex. *Medicine*, *95*, e3714. https://doi.org/10.1097/MD.0000000000003714

Crameri, F. (2023). Scientific colour maps (version 8.0.0). *Zenodo*. https://doi.org/https://doi.org/10.5281/zenodo.1243862

Dale, A. M., Fischl, B., & Sereno, M. I. (1999). Cortical surface-based analysis: I. Segmentation and surface reconstruction. *NeuroImage*, *9*, 179–194. https://doi.org/10.1006/nimg.1998.0395

Dandu, B., Shao, Y., & Visell, Y. (2021). Rendering spatiotemporal haptic effects via the physics of waves in the skin. *IEEE Transactions on Haptics*, *14*, 347–358. https://doi.org/10.1109/TOH.2020.3029768

Desikan, R. S., Ségonne, F., Fischl, B., Quinn, B. T., Dickerson, B. C., Blacker, D., Buckner, R. L., Dale, A. M., Maguire, R. P., Hyman, B. T., Albert, M. S., & Killiany, R. J. (2006). An automated labeling system for subdividing the human cerebral cortex on MRI scans into gyral based regions of interest. *NeuroImage*, *31*, 968–980. https://doi.org/10.1016/j.neuroimage.2006.01.021

DiCarlo, J. J., Johnson, K. O., & Hsiao, S. S. (1998). Structure of receptive fields in area 3b of primary somatosensory cortex in the alert monkey. *The Journal of Neuroscience*, *18*, 2626–2645. https://doi.org/10.1523/JNEUROSCI.18-07-02626.1998

Dumoulin, S. O., & Knapen, T. (2018). How visual cortical organization is altered by ophthalmologic and neurologic disorders. *Annual Review of Vision Science*, *4*, 357–379. https://doi.org/10.1146/annurev-vision-091517-033948

Dumoulin, S. O., & Wandell, B. A. (2008). Population receptive field estimates in human visual cortex. *NeuroImage*, *39*, 647–660. https://doi.org/10.1016/j.neuroimage.2007.09.034

Engel, S. A. (2012). The development and use of phase-encoded functional MRI designs. *NeuroImage*, *62*, 1195–1200. https://doi.org/10.1016/j.neuroimage.2011.09.059

Engel, S. A., Rumelhart, D. E., Wandell, B. A., Lee, A. T., Glover, G. H., Chichilnisky, E.-J., & Shadlen, M. N. (1994). fMRI of human visual cortex. *Nature*, *369*, 525–525. https://doi.org/10.1038/369525a0

Fischl, B., Rajendran, N., Busa, E., Augustinack, J., Hinds, O., Yeo, B. T. T., Mohlberg, H., Amunts, K., & Zilles, K. (2008). Cortical folding patterns and predicting cytoarchitecture. *Cerebral Cortex*, *18*, 1973–1980. https://doi.org/10.1093/cercor/bhm225

Fischl, B. (2012). FreeSurfer. *NeuroImage*, *62*, 774–781. https://doi.org/10.1016/j.neuroimage.2012.01.021

Fischl, B., Sereno, M. I., & Dale, A. M. (1999). Cortical surface-based analysis: II: Inflation, flattening, and a surface-based coordinate system. *NeuroImage*, *9*, 195–207. https://doi.org/10.1006/nimg.1998.0396

Fracasso, A., Petridou, N., & Dumoulin, S. O. (2016). Systematic variation of population receptive field properties across cortical depth in human visual cortex. *NeuroImage*, *139*, 427–438. https://doi.org/10.1016/j.neuroimage.2016.06.048

Gordon, E. M., Laumann, T. O., Gilmore, A. W., Newbold, D. J., Greene, D. J., Berg, J. J., Ortega, M., Hoyt-Drazen, C., Gratton, C., Sun, H., Hampton, J. M., Coalson, R. S., Nguyen, A. L., McDermott, K. B., Shimony, J. S., Snyder, A. Z., Schlaggar, B. L., Petersen, S. E., Nelson, S. M., & Dosenbach, N. U. (2017). Precision functional mapping of individual human brains. *Neuron*, *95*, 791–807.e7. https://doi.org/10.1016/j.neuron.2017.07.011

Gorgolewski, K. J., Auer, T., Calhoun, V. D., Craddock, R. C., Das, S., Duff, E. P., Flandin, G., Ghosh, S. S., Glatard, T., Halchenko, Y. O., Handwerker, D. A., Hanke, M., Keator, D., Li, X., Michael, Z., Maumet, C., Nichols, B. N., Nichols, T. E., Pellman, J., . . . Poldrack, R. A. (2016). The brain imaging data structure, a format for organizing and describing outputs of neuroimaging experiments. *Scientific Data*, *3*, 160044. https://doi.org/10.1038/sdata.2016.44

Gorniak, S. L., Khan, A., Ochoa, N., Sharma, M. D., & Phan, C. L. (2014). Detecting subtle fingertip sensory and motor dysfunction in adults with type II diabetes. *Experimental Brain Research*, *232*, 1283–1291. https://doi.org/10.1007/s00221-014-3844-x

Greve, D. N., & Fischl, B. (2009). Accurate and robust brain image alignment using boundary-based registration. *NeuroImage*, *48*, 63–72. https://doi.org/10.1016/j.neuroimage.2009.06.060

Hoopes, A., Mora, J. S., Dalca, A. V., Fischl, B., & Hoffmann, M. (2022). SynthStrip: Skull-stripping for any brain image. *NeuroImage*, *260*, 119474. https://doi.org/10.1016/j.neuroimage.2022.119474

In, M.-H., Posnansky, O., Beall, E. B., Lowe, M. J., & Speck, O. (2015). Distortion correction in EPI using an extended PSF method with a reversed phase gradient approach. *PLOS ONE*, *10*, e0116320. https://doi.org/10.1371/journal.pone.0116320

In, M.-H., & Speck, O. (2012). Highly accelerated PSF-mapping for EPI distortion correction with improved fidelity. *Magnetic Resonance Materials in Physics, Biology and Medicine*, *25*, 183–192. https://doi.org/10.1007/s10334-011-0275-6

Janko, D., Thoenes, K., Park, D., Willoughby, W. R., Horton, M., & Bolding, M. (2022). Somatotopic mapping of the fingers in the somatosensory cortex using functional magnetic resonance imaging: A review of literature. *Frontiers in Neuroanatomy*, *16*. https://doi.org/10.3389/fnana.2022.866848

Johnson, K. (2002). Neural basis of haptic perception. In H. Pashler & S. Yantis (Eds.), *Stevens' handbook of experimental psychology: Sensation and perception* (3rd ed., pp. 537–583). John Wiley & Sons Inc. https://doi.org/https://doi.org/10.1002/0471214426.pas0113

Kawaiah, A., Thakur, M., Garg, S., Kawasmi, S. H., & Hassan, A. (2020). Fingertip injuries and amputations: A review of the literature. *Cureus*, *12*, e8291. https://doi.org/10.7759/cureus.8291

Kim, S. S., Gomez-Ramirez, M., Thakur, P. H., & Hsiao, S. S. (2015). Multimodal interactions between proprioceptive and cutaneous signals in primary somatosensory cortex. *Neuron*, *86*, 555–566. https://doi.org/10.1016/j.neuron.2015.03.020

Kleiner, M., Brainard, D. H., & Pelli, D. G. (2007). What's new in Psychtoolbox-3? [ECVP abstract supplement]. *Perception*, *36*, 1–235. https://doi.org/10.1177/03010066070360S101

Klink, P. C., Chen, X., Vanduffel, W., & Roelfsema, P. R. (2021). Population receptive fields in nonhuman primates from whole-brain fMRI and large-scale neurophysiology in visual cortex. *eLife*, *10*, e67304. https://doi.org/10.7554/eLife.67304

Koopmans, P. J., Barth, M., & Norris, D. G. (2010). Layer-specific BOLD activation in human V1. *Human Brain Mapping*, *31*, 1297–1304. https://doi.org/10.1002/hbm.20936

Kriegeskorte, N., Simmons, W. K., Bellgowan, P. S. F., & Baker, C. I. (2009). Circular analysis in systems neuroscience: The dangers of double dipping. *Nature Neuroscience*, *12*, 535–540. https://doi.org/10.1038/nn.2303

Kuehn, E., Haggard, P., Villringer, A., Pleger, B., & Sereno, M. I. (2018). Visually-driven maps in area 3b. *The Journal of Neuroscience*, *38*, 1295–1310. https://doi.org/10.1523/JNEUROSCI.0491-17.2017

Lagarias, J. C., Reeds, J. A., Wright, M. H., & Wright, P. E. (1998). Convergence properties of the Nelder–Mead simplex method in low dimensions. *SIAM Journal on Optimization*, *9*, 112–147. https://doi.org/10.1137/S1052623496303470

Lazar, L., Chand, P., Rajan, R., Mohammed, H., & Jain, N. (2022). Somatosensory cortex of macaque monkeys is designed for opposable thumb. *Cerebral Cortex*, *33*, 195–206. https://doi.org/10.1093/cercor/bhac061

Lerma-Usabiaga, G., Benson, N., Winawer, J., & Wandell, B. A. (2020). A validation framework for neuroimaging software: The case of population receptive fields. *PLOS Computational Biology*, *16*, e1007924. https://doi.org/10.1371/journal.pcbi.1007924

Li, X., Morgan, P. S., Ashburner, J., Smith, J., & Rorden, C. (2016). The first step for neuroimaging data analysis: DICOM to NIfTI conversion. *Journal of Neuroscience Methods*, *264*, 47–56. https://doi.org/10.1016/j.jneumeth.2016.03.001

Liu, P., Chrysidou, A., Doehler, J., Hebart, M. N., Wolbers, T., & Kuehn, E. (2021). The organizational principles of de-differentiated topographic maps in somatosensory cortex. *eLife*, *10*, e60090. https://doi.org/10.7554/eLife.60090

Liu, P., Doehler, J., Henschke, J. U., Northall, A., Serian, A., Loaiza-Carvajal, L. C., Budinger, E., Schwarzkopf, D. S., Speck, O., Pakan, J. M., & Kuehn, E. (2025). Cortical sensory aging is layer-specific. *bioRxiv*. https://doi.org/10.1101/2023.12.01.567841

Liu, T. T. (2017). Reprint of 'noise contributions to the fMRI signal: An overview'. *NeuroImage*, *154*, 4–14. https://doi.org/10.1016/j.neuroimage.2017.05.031

Logothetis, N. K. (2003). The underpinnings of the BOLD functional magnetic resonance imaging signal. *The Journal of Neuroscience*, *23*, 3963–3971. https://doi.org/10.1523/JNEUROSCI.23-10-03963.2003

Lüsebrink, F., Mattern, H., Yakupov, R., Acosta-Cabronero, J., Ashtarayeh, M., Oeltze-Jafra, S., & Speck, O. (2021). Comprehensive ultrahigh resolution whole brain in vivo MRI dataset as a human phantom. *Scientific Data*, *8*, 138. https://doi.org/10.1038/s41597-021-00923-w

Lüsebrink, F., Sciarra, A., Mattern, H., Yakupov, R., & Speck, O. (2017). T1-weighted in vivo human whole brain MRI dataset with an ultrahigh isotropic resolution of 250 μm. *Scientific Data*, *4*, 170032. https://doi.org/10.1038/sdata.2017.32

Lynch, P. J. (2006). Brain human lateral view. *Wikimedia*. https://commons.wikimedia.org/wiki/File:Brain_human_lateral_view.svg

Maclaren, J., Armstrong, B. S. R., Barrows, R. T., Danishad, K. A., Ernst, T., Foster, C. L., Gumus, K., Herbst, M., Kadashevich, I. Y., Kusik, T. P., Li, Q., Lovell-Smith, C., Prieto, T., Schulze, P., Speck, O., Stucht, D., & Zaitsev, M. (2012). Measurement and correction of microscopic head motion during magnetic resonance imaging of the brain. *PLoS ONE*, *7*, e48088. https://doi.org/10.1371/journal.pone.0048088

Manfredi, L. R., Baker, A. T., Elias, D. O., Dammann, J. F., Zielinski, M. C., Polashock, V. S., & Bensmaia, S. J. (2012). The effect of surface wave propagation on neural responses to vibration in primate glabrous skin. *PLoS ONE*, *7*, e31203. https://doi.org/10.1371/journal.pone.0031203

Merzenich, M. M., Kaas, J. H., Sur, M., & Lin, C.-S. (1978). Double representation of the body surface within cytoarchitectonic area 3b and 1 in "SI" in the owl monkey (Aotus trivirgatus). *Journal of Comparative Neurology*, *181*, 41–73. https://doi.org/10.1002/cne.901810104

Merzenich, M. M., Nelson, R. J., Kaas, J. H., Stryker, M. P., Jenkins, W. M., Zook, J. M., Cynader, M. S., & Schoppmann, A. (1987). Variability in hand surface representations in areas 3b and 1 in adult owl and squirrel monkeys. *Journal of Comparative Neurology*, *258*, 281–296. https://doi.org/10.1002/CNE.902580208

Mugler, J. P., & Brookeman, J. R. (1990). Three-dimensional magnetization-prepared rapid gradient-echo imaging (3D MP RAGE). *Magnetic Resonance in Medicine*, *15*, 152–157. https://doi.org/10.1002/mrm.1910150117

Naselaris, T., Kay, K. N., Nishimoto, S., & Gallant, J. L. (2011). Encoding and decoding in fMRI. *NeuroImage*, *56*, 400–410. https://doi.org/10.1016/j.neuroimage.2010.07.073

Nelder, J. A., & Mead, R. (1965). A simplex method for function minimization. *The Computer Journal*, *7*, 308–313. https://doi.org/10.1093/comjnl/7.4.308

Nelson, R. J., Sur, M., Felleman, D. J., & Kaas, J. H. (1980). Representations of the body surface in postcentral parietal cortex of Macaca fascicularis. *Journal of Comparative Neurology*, *192*, 611–643. https://doi.org/10.1002/cne.901920402

Nora, D. B., Becker, J., Ehlers, J. A., & Gomes, I. (2004). Clinical features of 1039 patients with neurophysiological diagnosis of carpal tunnel syndrome. *Clinical Neurology and Neurosurgery*, *107*, 64–69. https://doi.org/10.1016/j.clineuro.2004.08.003

Overduin, S. A., & Servos, P. (2004). Distributed digit somatotopy in primary somatosensory cortex. *NeuroImage*, *23*, 462–472. https://doi.org/10.1016/j.neuroimage.2004.06.024

Overduin, S. A., & Servos, P. (2008). Symmetric sensorimotor somatotopy. *PLoS ONE*, *3*, e1505. https://doi.org/10.1371/journal.pone.0001505

Pelli, D. G. (1997). The VideoToolbox software for visual psychophysics: Transforming numbers into movies. *Spatial Vision*, *10*, 437–442. https://doi.org/10.1163/156856897X00366

Pernet, C. R. (2014). Misconceptions in the use of the general linear model applied to functional MRI: A tutorial for junior neuro-imagers. *Frontiers in Neuroscience*, *8*, 1. https://doi.org/10.3389/fnins.2014.00001

Polimeni, J. R., Fischl, B., Greve, D. N., & Wald, L. L. (2010). Laminar analysis of 7T BOLD using an imposed spatial activation pattern in human V1. *NeuroImage*, *52*, 1334–1346. https://doi.org/10.1016/j.neuroimage.2010.05.005

Polimeni, J. R., Renvall, V., Zaretskaya, N., & Fischl, B. (2018). Analysis strategies for high-resolution UHF-fMRI data. *NeuroImage*, *168*, 296–320. https://doi.org/10.1016/j.neuroimage.2017.04.053

Puckett, A. M., Bollmann, S., Junday, K., Barth, M., & Cunnington, R. (2020). Bayesian population receptive field modeling in human somatosensory cortex. *NeuroImage*, *208*, 116465. https://doi.org/10.1016/j.neuroimage.2019.116465

Puckett, A. M., & Sanchez-Panchuelo, R. M. (2023). Imaging somatosensory cortex: Human functional magnetic resonance imaging (fMRI). In N. P. Holmes (Ed.), *Somatosensory research methods* (pp. 397–430). Springer US. https://doi.org/10.1007/978-1-0716-3068-6_18

Rossum, G. V., & Drake, F. L. (2009). *Python 3 reference manual*. CreateSpace.

Sanchez-Panchuelo, R. M., Francis, S., Bowtell, R., & Schluppeck, D. (2010). Mapping human somatosensory cortex in individual subjects with 7T functional MRI. *Journal of Neurophysiology*, *103*, 2544–2556. https://doi.org/10.1152/JN.01017.2009

Sanchez-Panchuelo, R. M., Besle, J., Beckett, A., Bowtell, R., Schluppeck, D., & Francis, S. (2012). Within-digit functional parcellation of Brodmann areas of the human primary somatosensory cortex using functional magnetic resonance imaging at 7 Tesla. *The Journal of Neuroscience*, *32*, 15815–15822. https://doi.org/10.1523/JNEUROSCI.2501-12.2012

Sanchez-Panchuelo, R. M., Besle, J., Schluppeck, D., Humberstone, M., & Francis, S. (2018). Somatotopy in the human somatosensory system. *Frontiers in Human Neuroscience*, *12*, 235. https://doi.org/10.3389/fnhum.2018.00235

Schellekens, W., Thio, M., Badde, S., Winawer, J., Ramsey, N., & Petridou, N. (2021). A touch of hierarchy: Population receptive fields reveal fingertip integration in Brodmann areas in human primary somatosensory cortex. *Brain Structure and Function*, *226*, 2099–2112. https://doi.org/10.1007/s00429-021-02309-5

Schwarzkopf, D. S. (2023). SamSrf IX - Matlab toolbox for pRF & CF analysis (version 9.51). https://doi.org/https://doi.org/10.17605/OSF.IO/2RGSM

Schweisfurth, M. A., Frahm, J., & Schweizer, R. (2014). Individual fMRI maps of all phalanges and digit bases of all fingers in human primary somatosensory cortex. *Frontiers in Human Neuroscience*, *8*, 658. https://doi.org/10.3389/fnhum.2014.00658

Schweisfurth, M. A., Frahm, J., & Schweizer, R. (2015). Individual left-hand and right-hand intra-digit representations in human primary somatosensory cortex. *European Journal of Neuroscience*, *42*, 2155–2163. https://doi.org/10.1111/ejn.12978

Senden, M., Reithler, J., Gijsen, S., & Goebel, R. (2014). Evaluating population receptive field estimation frameworks in terms of robustness and reproducibility. *PLoS ONE*, *9*, e114054. https://doi.org/10.1371/journal.pone.0114054

Sereno, M. I., Sood, M. R., & Huang, R.-S. (2022). Topological maps and brain computations from low to high. *Frontiers in Systems Neuroscience*, *16*, 787737. https://doi.org/10.3389/fnsys.2022.787737

Shmuel, A., Yacoub, E., Pfeuffer, J., Van de Moortele, P. F., Adriany, G., Hu, X., & Ugurbil, K. (2002). Sustained negative BOLD, blood flow and oxygen consumption response and its coupling to the positive response in the human brain. *Neuron*, *36*, 1195–1210. https://doi.org/10.1016/s0896-6273(02)01061-9

Sofia, K. O., & Jones, L. (2013). Mechanical and psychophysical studies of surface wave propagation during vibrotactile stimulation. *IEEE Transactions on Haptics*, *6*, 320–329. https://doi.org/10.1109/TOH.2013.1

Stoll, S., Finlayson, N. J., & Schwarzkopf, D. S. (2020). Topographic signatures of global object perception in human visual cortex. *NeuroImage*, *220*, 116926. https://doi.org/10.1016/j.neuroimage.2020.116926

Stoll, S., Infanti, E., de Haas, B., & Schwarzkopf, D. S. (2022). Pitfalls in post hoc analyses of population receptive field data. *NeuroImage*, *263*, 119557. https://doi.org/10.1016/j.neuroimage.2022.119557

Stucht, D., Danishad, K. A., Schulze, P., Godenschweger, F., Zaitsev, M., & Speck, O. (2015). Highest resolution in vivo human brain MRI using prospective motion correction. *PLOS ONE*, *10*, e0133921. https://doi.org/10.1371/journal.pone.0133921

Sur, M., Merzenich, M. M., & Kaas, J. H. (1980). Magnification, receptive-field area, and "hypercolumn" size in areas 3b and 1 of somatosensory cortex in owl monkeys. *Journal of Neurophysiology*, *44*, 295–311. https://doi.org/10.1152/jn.1980.44.2.295

Tal, Z., Geva, R., & Amedi, A. (2017). Positive and negative somatotopic BOLD responses in contralateral versus ipsilateral Penfield homunculus. *Cerebral Cortex*, *27*, 962–980. https://doi.org/10.1093/cercor/bhx024

The FIL Methods Group. (2021). *SPM12 manual*. https://www.fil.ion.ucl.ac.uk/spm/

The MathWorks Inc. (2015). Matlab (version R2015b 8.6). https://www.mathworks.com

The MathWorks Inc. (2022). Matlab (version R2022b 9.13). https://www.mathworks.com

Tian, Q., Bilgic, B., Fan, Q., Ngamsombat, C., Zaretskaya, N., Fultz, N. E., Ohringer, N. A., Chaudhari, A. S., Hu, Y., Witzel, T., Setsompop, K., Polimeni, J. R., & Huang, S. Y. (2021). Improving in vivo human cerebral cortical surface reconstruction using data-driven super-resolution. *Cerebral Cortex*, *31*, 463–482. https://doi.org/10.1093/cercor/bhaa237

Tian, Q., Zaretskaya, N., Fan, Q., Ngamsombat, C., Bilgic, B., Polimeni, J. R., & Huang, S. Y. (2021). Improved cortical surface reconstruction using sub-millimeter resolution MPRAGE by image denoising. *NeuroImage*, *233*, 117946. https://doi.org/10.1016/j.neuroimage.2021.117946

Trzcinski, N. K., Hsiao, S. S., Connor, C. E., & Gomez-Ramirez, M. (2023). Multi-finger receptive field properties in primary somatosensory cortex: A revised account of the spatiotemporal integration functions of area 3b. *Cell Reports*, *42*, 112176. https://doi.org/10.1016/j.celrep.2023.112176

Tummala, N., Reardon, G., Dandu, B., Shao, Y., Saal, H. P., & Visell, Y. (2024). Biomechanical filtering supports tactile encoding efficiency in the human hand. *bioRxiv*. https://doi.org/10.1101/2023.11.10.565040

Tustison, N. J., Cook, P. A., Holbrook, A. J., Johnson, H. J., Muschelli, J., Devenyi, G. A., Duda, J. T., Das, S. R., Cullen, N. C., Gillen, D. L., Yassa, M. A., Stone, J. R., Gee, J. C., & Avants, B. B. (2021). The ANTsX ecosystem for quantitative biological and medical imaging. *Scientific Reports*, *11*, 9068. https://doi.org/10.1038/s41598-021-87564-6

Welvaert, M., & Rosseel, Y. (2014). A review of fMRI simulation studies. *PLoS ONE*, *9*, e101953. https://doi.org/10.1371/journal.pone.0101953

Yousry, T., Schmid, U., Alkadhi, H., Schmidt, D., Peraud, A., Buettner, A., & Winkler, P. (1997). Localization of the motor hand area to a knob on the precentral gyrus. A new landmark. *Brain*, *120*, 141–157. https://doi.org/10.1093/brain/120.1.141

Zaitsev, M., Hennig, J., & Speck, O. (2004). Point spread function mapping with parallel imaging techniques and high acceleration factors: Fast, robust, and flexible method for echo-planar imaging distortion correction. *Magnetic Resonance in Medicine*, *52*, 1156–1166. https://doi.org/10.1002/mrm.20261

Zaitsev, M., Maclaren, J., & Herbst, M. (2015). Motion artifacts in MRI: A complex problem with many partial solutions. *Journal of Magnetic Resonance Imaging*, *42*, 887–901. https://doi.org/10.1002/jmri.24850

Zeidman, P., Silson, E. H., Schwarzkopf, D. S., Baker, C. I., & Penny, W. (2018). Bayesian population receptive field modelling. *NeuroImage*, *180 (Part A)*, 173–187. https://doi.org/10.1016/j.neuroimage.2017.09.008

Zhang, R.-Y., Wei, X.-X., & Kay, K. (2020). Understanding multivariate brain activity: Evaluating the effect of voxelwise noise correlations on population codes in functional magnetic resonance imaging. *PLOS Computational Biology*, *16*, e1008153. https://doi.org/10.1371/journal.pcbi.1008153

Supplementary material

Supplementary figures

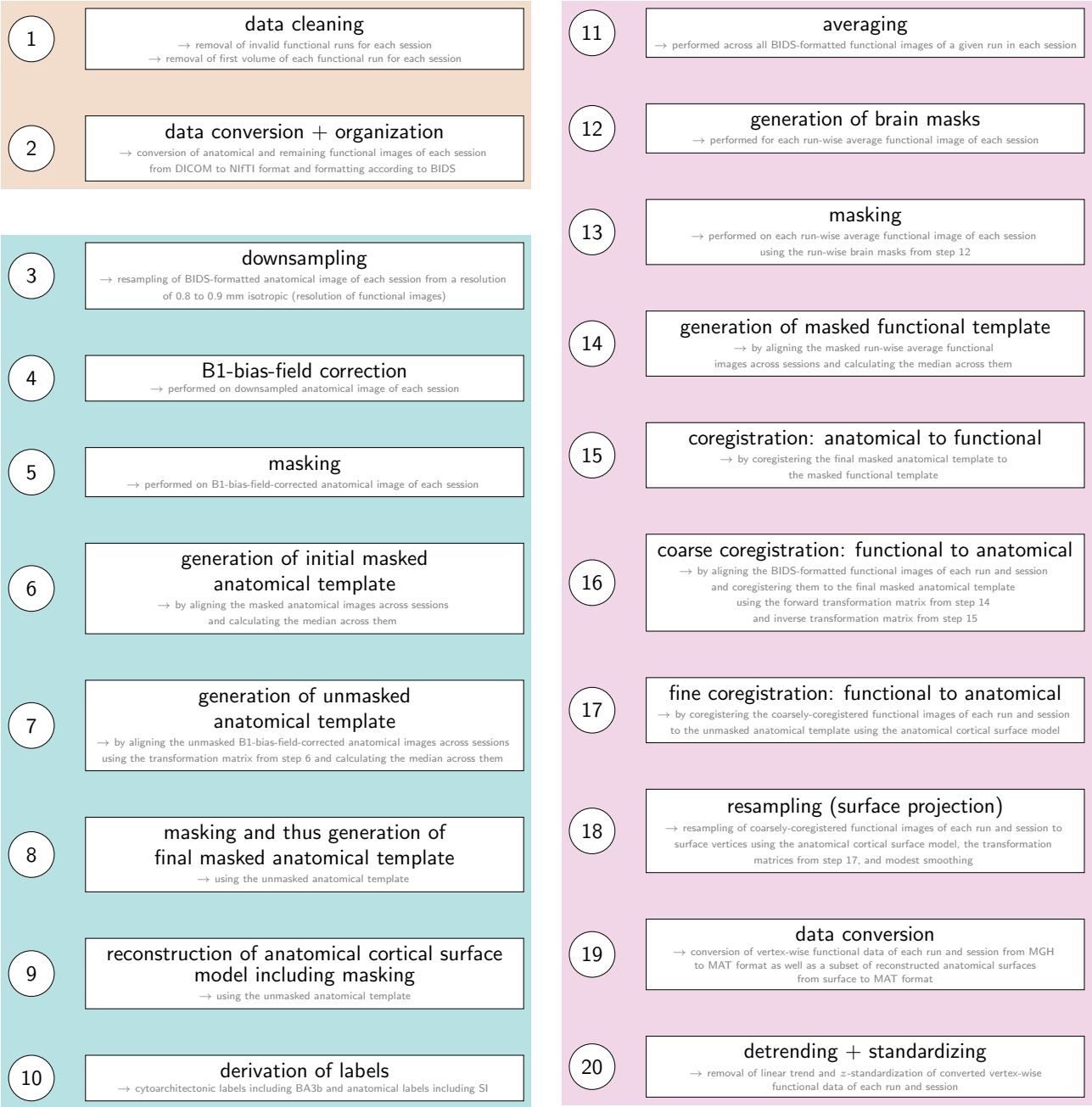

Figure S1. **Overview of performed preprocessing steps.** Tan box: Preparatory steps. Teal blue box: Preprocessing of anatomical data. Thistle box: Preprocessing of functional data. BA3b = Brodmann area 3b. SI = primary somatosensory cortex. BIDS = Brain Imaging Data Structure.

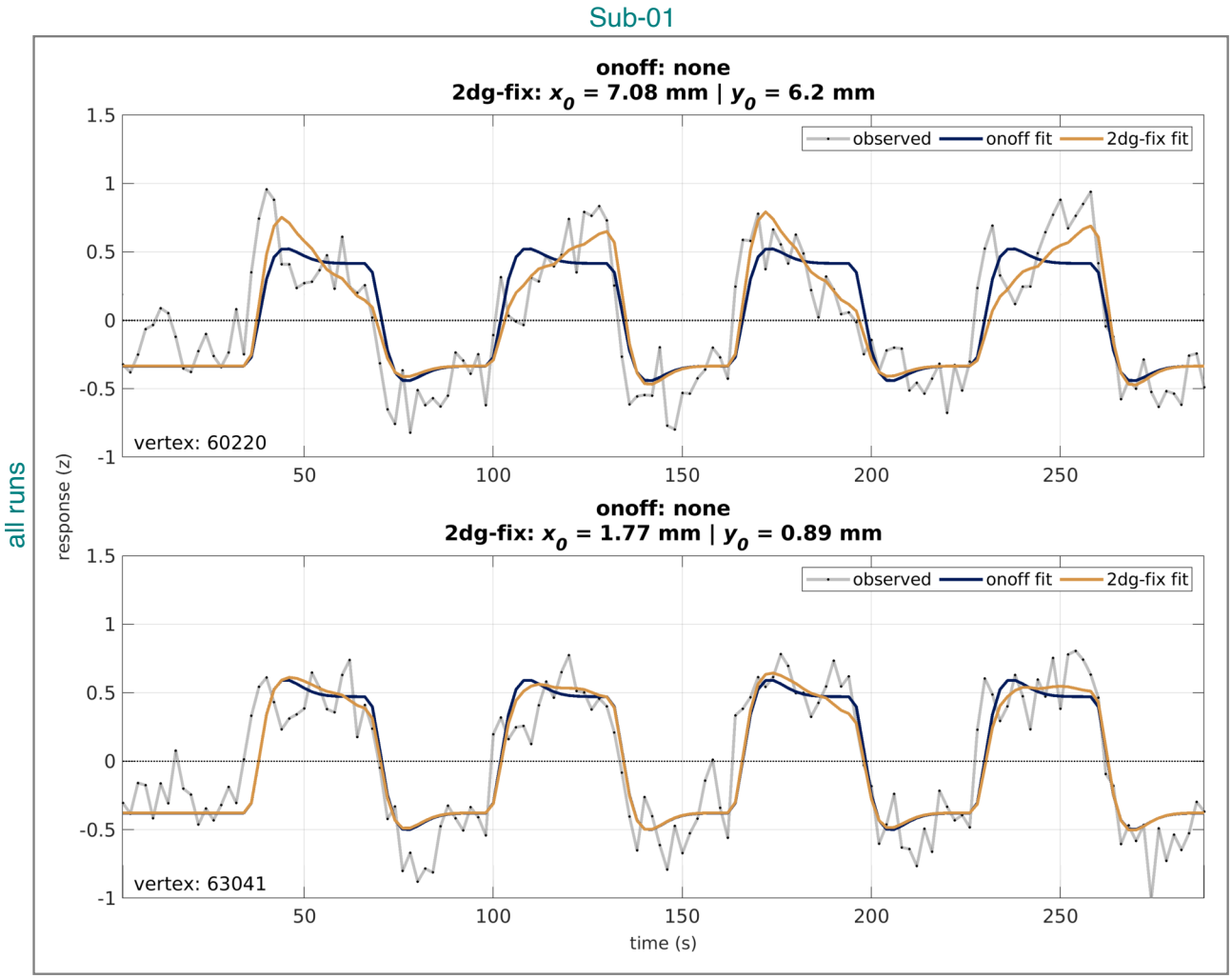

Figure S2. **Observed and fitted time courses corresponding to the onoff and 2dg-fix model for Sub-01 and all runs.** The time courses are based on data from session 2-4. Two example vertices from the identified BA3b cluster are displayed (vertex identifier is shown on bottom left of each panel). Headers in each panel list pRF position estimates (if available) for each model. Sub-01 = Subject 01. 2dg-fix = 2D Gaussian pRF model with parameter for pRF size fixed and constrained grid search. onoff = pRF model without any spatial tuning that simply reflects the presence or absence of tactile stimulation. pRF = population receptive field. BA3b = Brodmann area 3b.

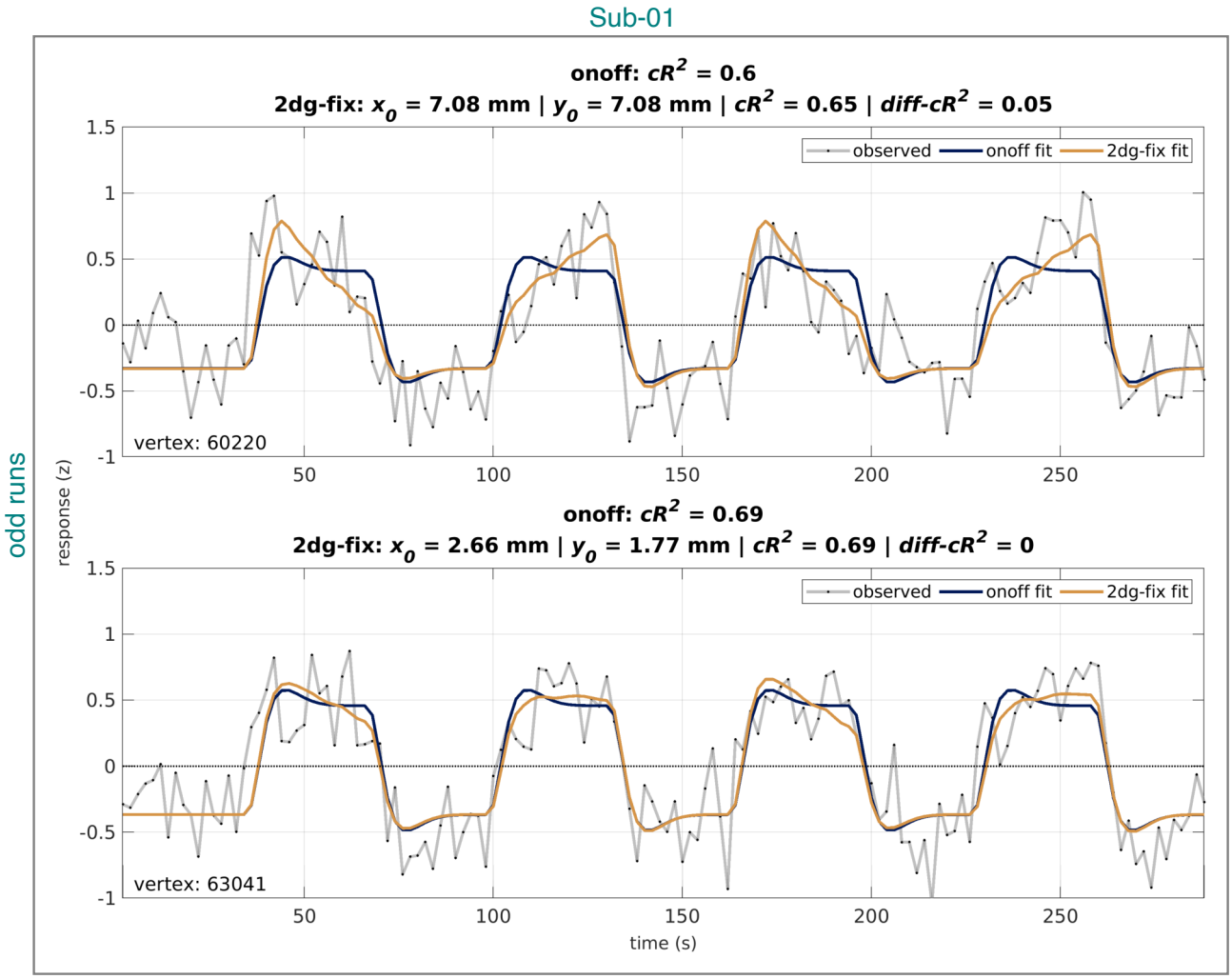

Figure S3. **Observed and fitted time courses corresponding to the onoff and 2dg-fix model for Sub-01 and the odd runs.** The time courses are based on data from session 2-4. Two example vertices from the identified BA3b cluster are displayed (vertex identifier is shown on bottom left of each panel). Headers in each panel list pRF position estimates (if available) and cross-validated goodness-of-fit measures for each model. Sub-01 = Subject 01. 2dg-fix = 2D Gaussian pRF model with parameter for pRF size fixed and constrained grid search. onoff = pRF model without any spatial tuning that simply reflects the presence or absence of tactile stimulation. pRF = population receptive field. *diff-*cR^2 = differential cR^2. BA3b = Brodmann area 3b.

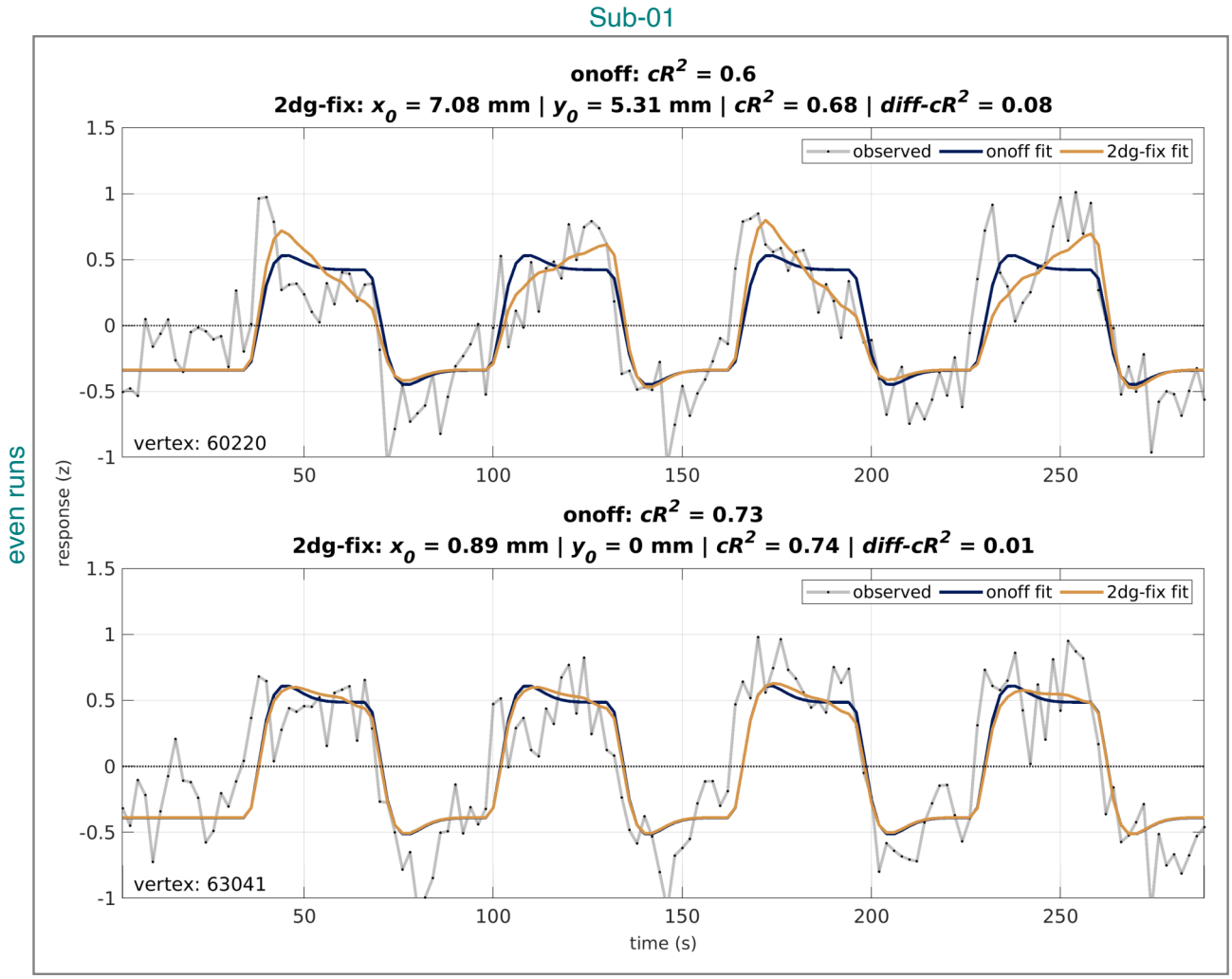

Figure S4. **Observed and fitted time courses corresponding to the onoff and 2dg-fix model for Sub-01 and the even runs.** The time courses are based on data from session 2-4. Two example vertices from the identified BA3b cluster are displayed (vertex identifier is shown on bottom left of each panel). Headers in each panel list pRF position estimates (if available) and cross-validated goodness-of-fit measures for each model. Sub-01 = Subject 01. 2dg-fix = 2D Gaussian pRF model with parameter for pRF size fixed and constrained grid search. onoff = pRF model without any spatial tuning that simply reflects the presence or absence of tactile stimulation. pRF = population receptive field. *diff-*cR^2 = differential cR^2. BA3b = Brodmann area 3b.

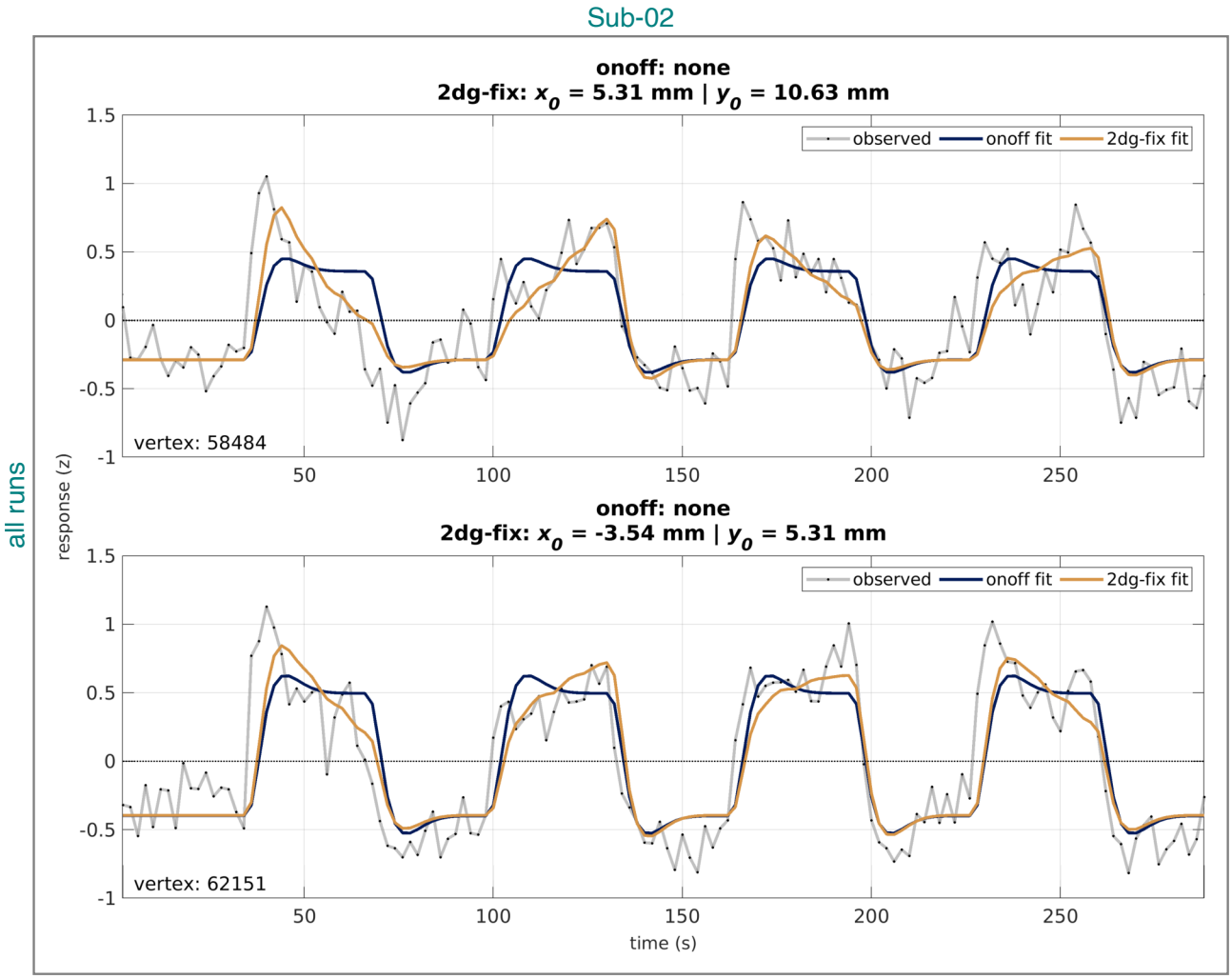

Figure S5. **Observed and fitted time courses corresponding to the onoff and 2dg-fix model for Sub-02 and all runs.** The time courses are based on data from session 2-4. Two example vertices from the identified BA3b cluster are displayed (vertex identifier is shown on bottom left of each panel). Headers in each panel list pRF position estimates (if available) for each model. Sub-02 = Subject 02. 2dg-fix = 2D Gaussian pRF model with parameter for pRF size fixed and constrained grid search. onoff = pRF model without any spatial tuning that simply reflects the presence or absence of tactile stimulation. pRF = population receptive field. BA3b = Brodmann area 3b.

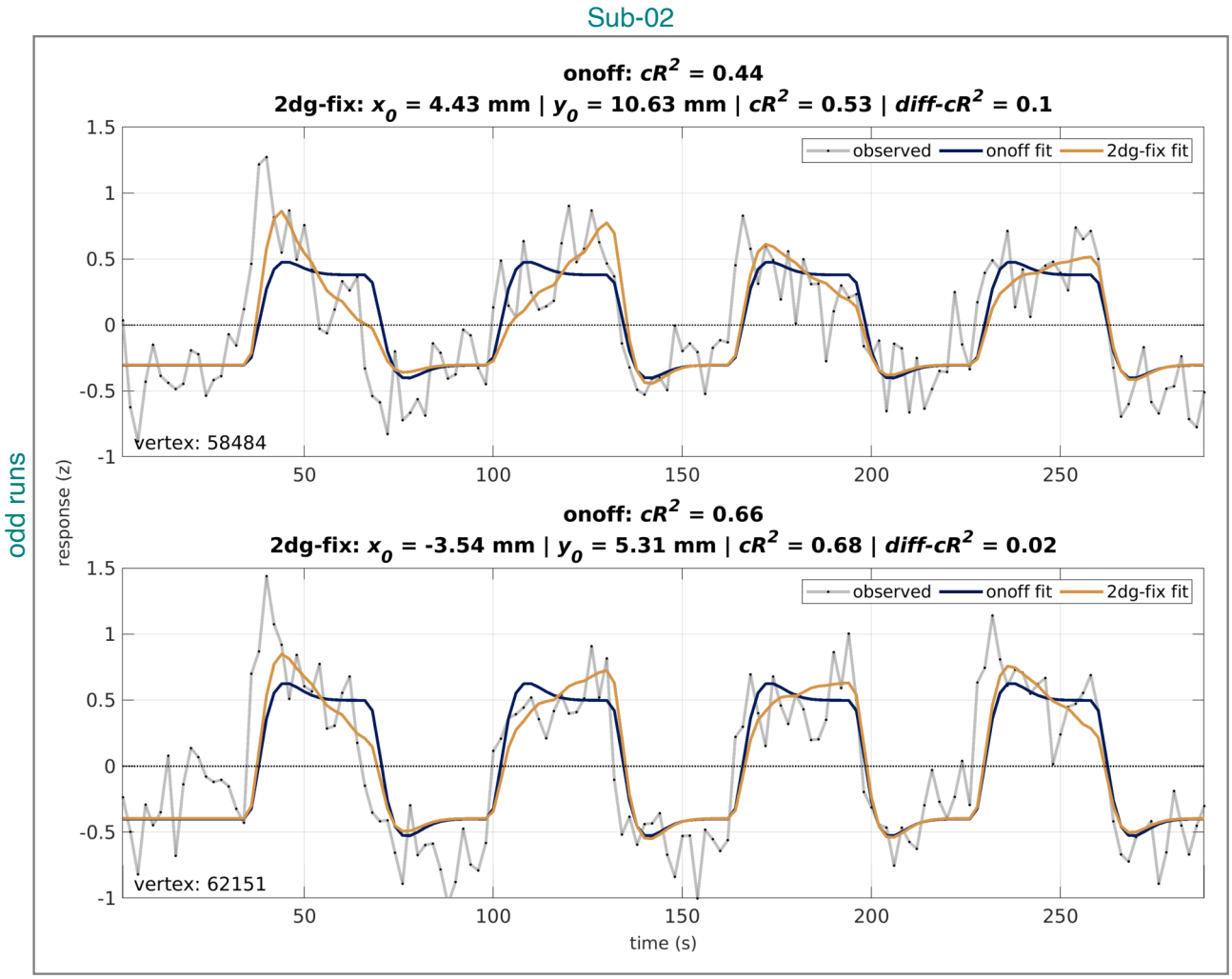

Figure S6. **Observed and fitted time courses corresponding to the onoff and 2dg-fix model for Sub-02 and the odd runs.** The time courses are based on data from session 2-4. Two example vertices from the identified BA3b cluster are displayed (vertex identifier is shown on bottom left of each panel). Headers in each panel list pRF position estimates (if available) and cross-validated goodness-of-fit measures for each model. Sub-02 = Subject 02. 2dg-fix = 2D Gaussian pRF model with parameter for pRF size fixed and constrained grid search. onoff = pRF model without any spatial tuning that simply reflects the presence or absence of tactile stimulation. pRF = population receptive field. *diff-*cR^2 = differential cR^2. BA3b = Brodmann area 3b.

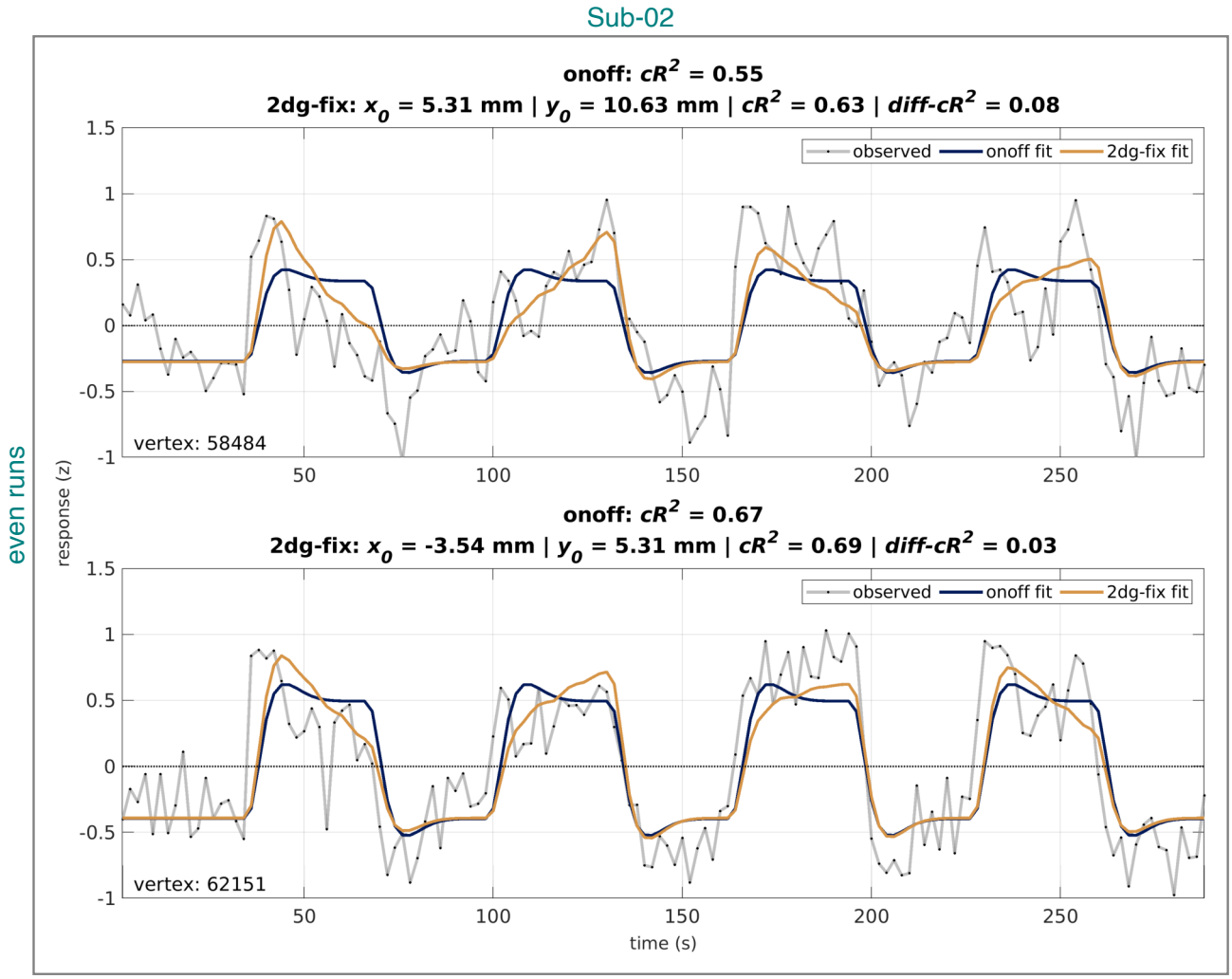

Figure S7. **Observed and fitted time courses corresponding to the onoff and 2dg-fix model for Sub-02 and the even runs.** The time courses are based on data from session 2-4. Two example vertices from the identified BA3b cluster are displayed (vertex identifier is shown on bottom left of each panel). Headers in each panel list pRF position estimates (if available) and cross-validated goodness-of-fit measures for each model. Sub-02 = Subject 02. 2dg-fix = 2D Gaussian pRF model with parameter for pRF size fixed and constrained grid search. onoff = pRF model without any spatial tuning that simply reflects the presence or absence of tactile stimulation. pRF = population receptive field. *diff-*cR^2 = differential cR^2. BA3b = Brodmann area 3b.

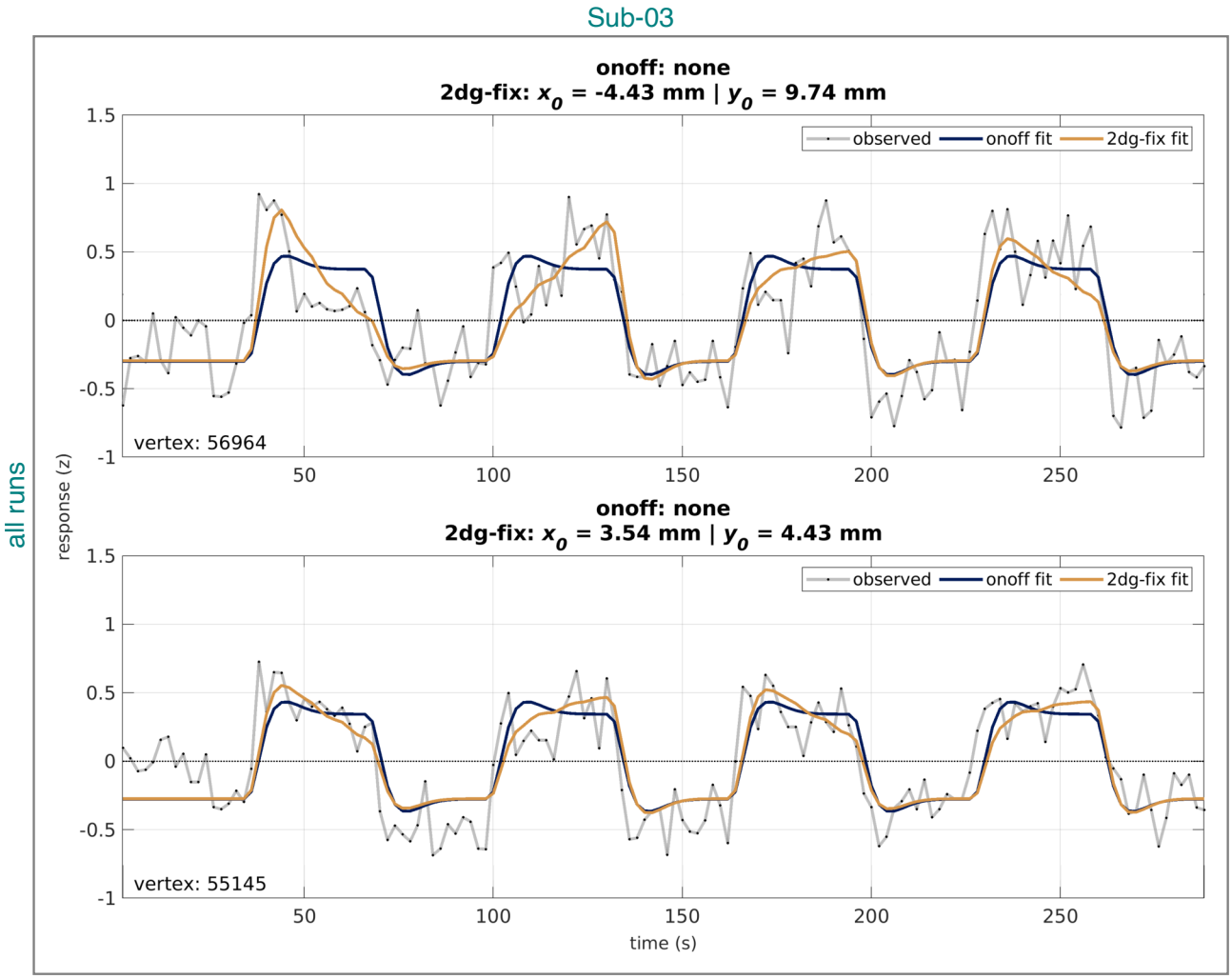

Figure S8. **Observed and fitted time courses corresponding to the onoff and 2dg-fix model for Sub-03 and all runs.** The time courses are based on data from session 2-4. Two example vertices from the identified BA3b cluster are displayed (vertex identifier is shown on bottom left of each panel). Headers in each panel list pRF position estimates (if available) for each model. Sub-03 = Subject 03. 2dg-fix = 2D Gaussian pRF model with parameter for pRF size fixed and constrained grid search. onoff = pRF model without any spatial tuning that simply reflects the presence or absence of tactile stimulation. pRF = population receptive field. BA3b = Brodmann area 3b.

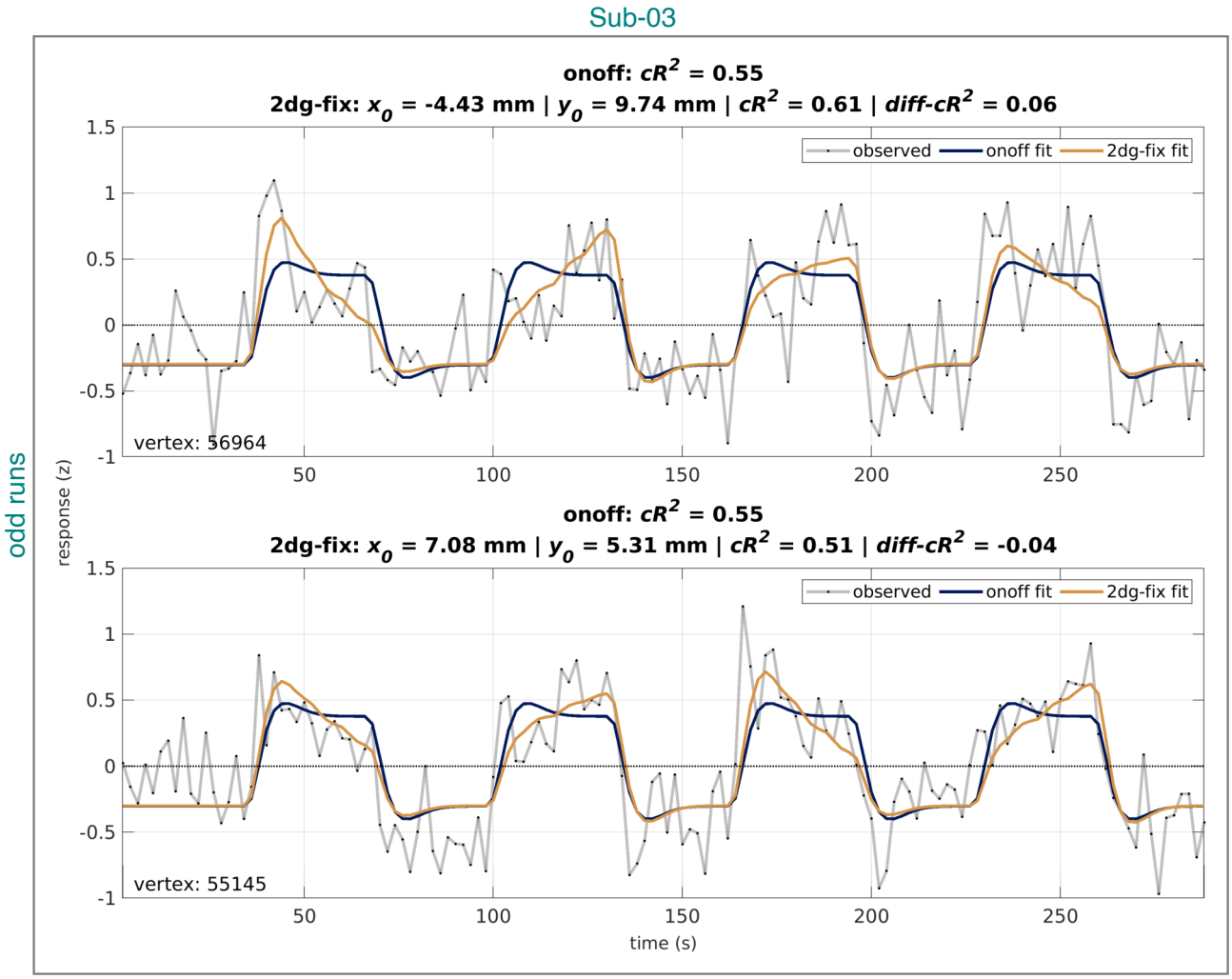

Figure S9. **Observed and fitted time courses corresponding to the onoff and 2dg-fix model for Sub-03 and the odd runs.** The time courses are based on data from session 2-4. Two example vertices from the identified BA3b cluster are displayed (vertex identifier is shown on bottom left of each panel). Headers in each panel list pRF position estimates (if available) and cross-validated goodness-of-fit measures for each model. Sub-03 = Subject 03. 2dg-fix = 2D Gaussian pRF model with parameter for pRF size fixed and constrained grid search. onoff = pRF model without any spatial tuning that simply reflects the presence or absence of tactile stimulation. pRF = population receptive field. *diff-*cR^2 = differential cR^2. BA3b = Brodmann area 3b.

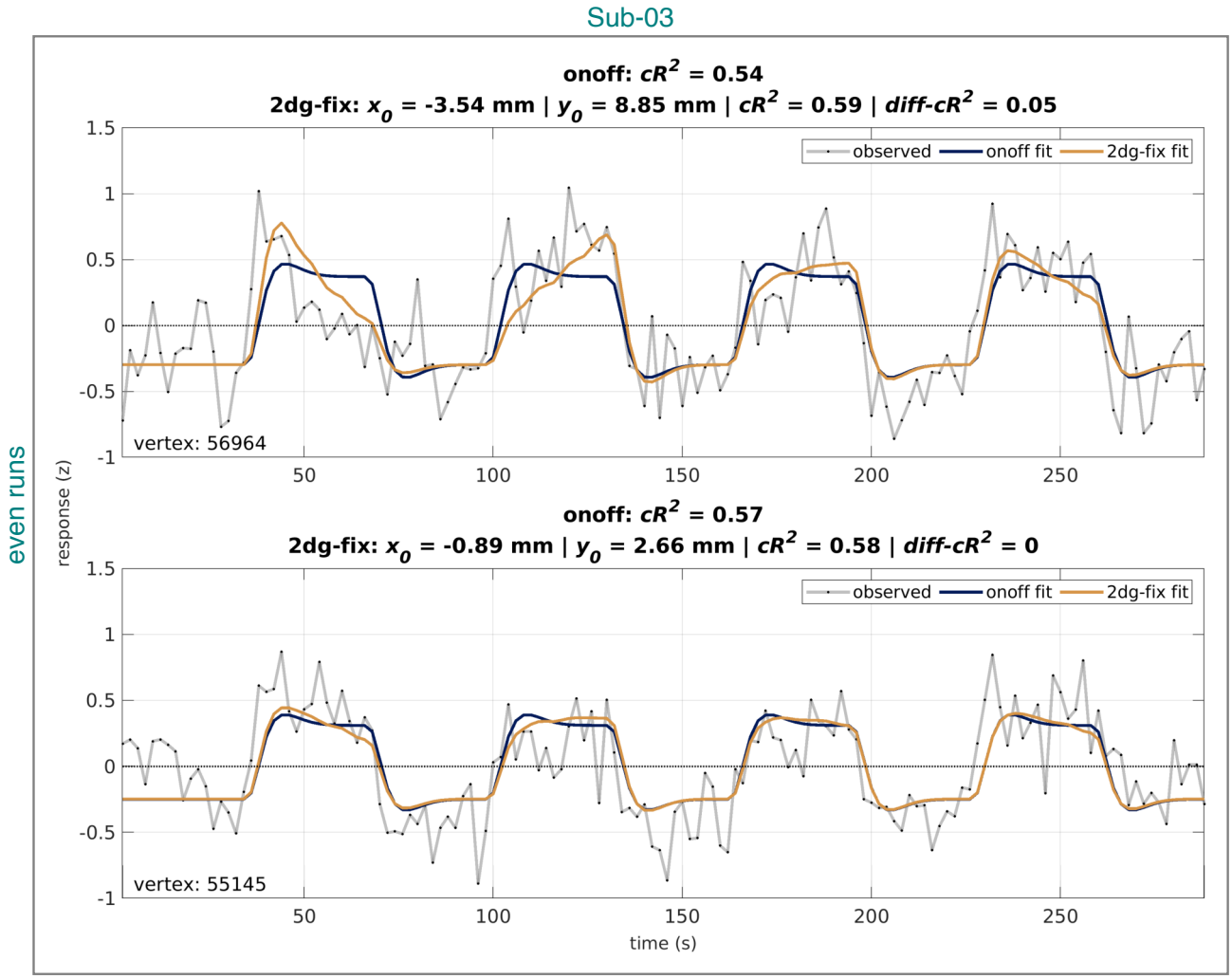

Figure S10. **Observed and fitted time courses corresponding to the onoff and 2dg-fix model for Sub-03 and the even runs.** The time courses are based on data from session 2-4. Two example vertices from the identified BA3b cluster are displayed (vertex identifier is shown on bottom left of each panel). Headers in each panel list pRF position estimates (if available) and cross-validated goodness-of-fit measures for each model. Sub-03 = Subject 03. 2dg-fix = 2D Gaussian pRF model with parameter for pRF size fixed and constrained grid search. onoff = pRF model without any spatial tuning that simply reflects the presence or absence of tactile stimulation. pRF = population receptive field. *diff-*cR^2 = differential cR^2. BA3b = Brodmann area 3b.

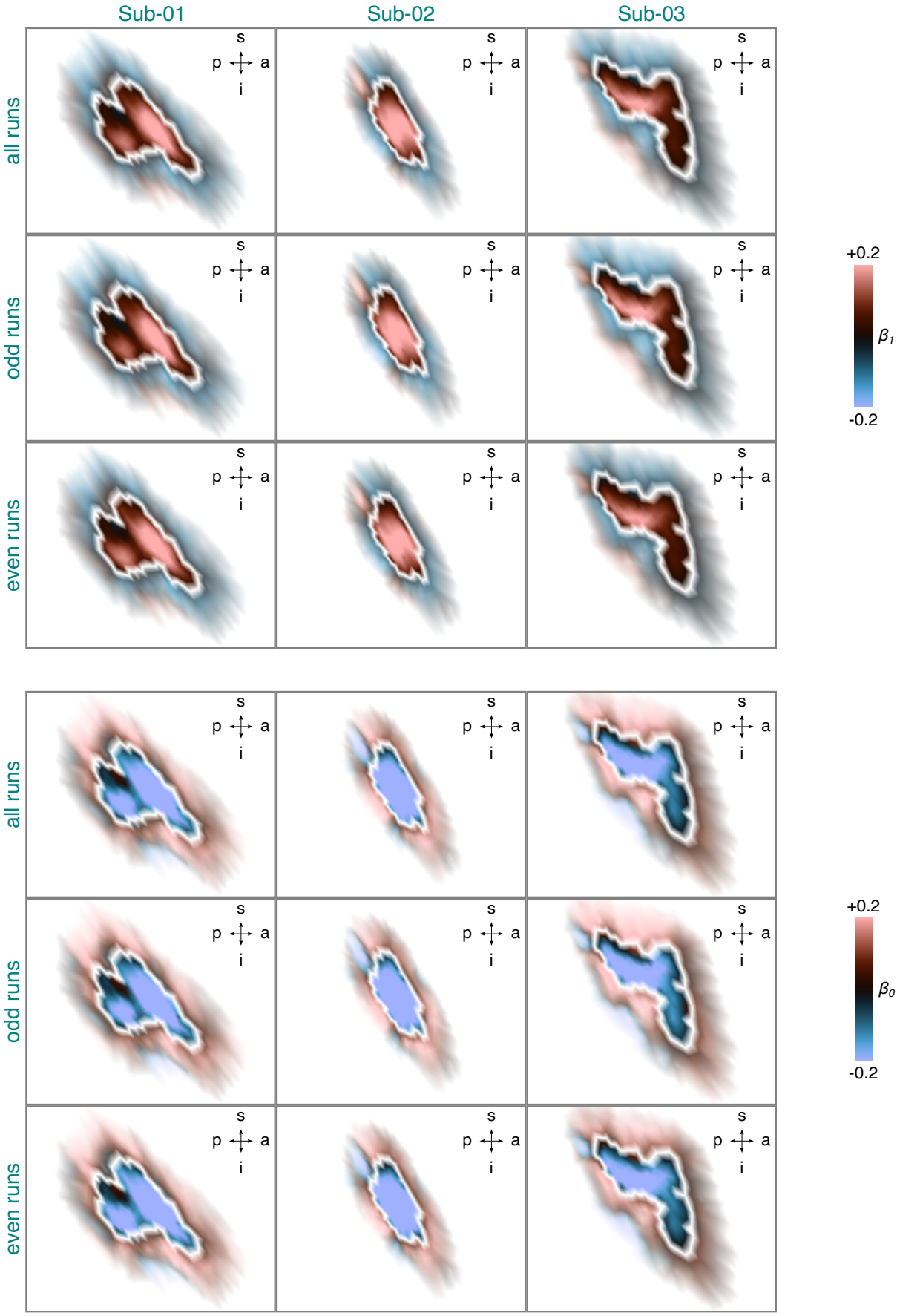

Figure S11. **PRF amplitude and baseline estimates for the identified BA3b cluster and the 2dg-fix model per participant and dataset.** The β_0 and β_1 estimates are based on data from session 2-4. They were projected onto an inflated cortical surface model where dark gray regions represent sulci and light gray regions gyri. A zoomed-in view is shown here. Any β_0 and β_1 estimates surpassing a value of ± 0.2 were set to this value. White lines denote the extent of the identified BA3b cluster (see Figure 4). BA3b = Brodmann area 3b. s = superior. p = posterior. i = inferior. a = anterior. Sub-01, Sub-02, Sub-03 = subject 01, 02, and 03. 2dg-fix = 2D Gaussian pRF model with parameter for pRF size fixed and constrained grid search. pRF = population receptive field.

Supplementary tables

Table S1
System Environment, Software Tool, and Notes as a Function of Implemented Procedure

Implemented procedure	System environment (version)	Software tool (version)	Notes (not available in main text)
Experiment	Windows 7		
		Matlab R2015b (8.6)[1]	
		PTB (3.0.11)[2]	
		QuaeroSys software[3]	
Preprocessing (preparation)	Ubuntu (22.04.2 LTS)		
Data cleaning	Bash (5.1.16)		
Data conversion + organization	Bash (5.1.16)	Python (3.10.12)[4]	
		dcm2niix (v1.0.20220720)[5]	
		dcm2bids (2.1.6)[6]	
Preprocessing (anatomical data)	Ubuntu (22.04.2 LTS)		
Downsampling	Bash (5.1.16)	FreeSurfer (7.3.2)[7]	mri_convert
B1-bias-field correction	Bash (5.1.16)	Matlab R2022b (9.13)[8]	
	Bash (5.1.16)	SPM12 (7771)[9]	FWHM: 15
			Reg.: 0.001
			Sampl. dist.: 2
Masking	Bash (5.1.16)	FreeSurfer (7.3.2)	mri_synthstrip
Generation of initial masked anatomical template	Bash (5.1.16)	ANTs (2.3.5)[10]	Trans. model: rigid
			Sim. metric: MI
Generation of unmasked anatomical template	Bash (5.1.16)	ANTs (2.3.5)	
Masking and thus generation of final masked anatomical template	Bash (5.1.16)	FreeSurfer (7.3.2)	mri_synthstrip
Reconstruction of anatomical cortical surface model including masking	Bash (5.1.16)	FreeSurfer (7.3.2)	recon-all with -hires
			mri_synthstrip with –no-csf
Derivation of labels	Bash (5.1.16)	FreeSurfer (7.3.2)	mri_annotation2label with
			rh.aparc.annot and lh.aparc.annot
Preprocessing (functional data)	Ubuntu (22.04.2 LTS)		
Averaging	Bash (5.1.16)	ANTs (2.3.5)	
Generation of brain masks	Bash (5.1.16)	ANTs (2.3.5)	
Masking	Bash (5.1.16)	ANTs (2.3.5)	
Generation of masked functional template	Bash (5.1.16)	ANTs (2.3.5)	Trans. model: rigid
			Sim. metric: MI
Coregistration: anatomical to functional	Bash (5.1.16)	ANTs (2.3.5)	Trans. type: rigid (stage 1)
Coarse coregistration: functional to anatomical	Bash (5.1.16)	ANTs (2.3.5)	
Fine coregistration: functional to anatomical	Bash (5.1.16)	FreeSurfer (7.3.2)	bbregister with –init-header; –bold
Resampling (surface projection)	Bash (5.1.16)	FreeSurfer (7.3.2)	mri_vol2surf
Data conversion		Matlab R2022b (9.13)	
		SamSrf (9.51)[11]	
Detrending + standardizing		Matlab R2022b (9.13)	
		SamSrf (9.51)	
Functional localization (analysis and visualization)	Ubuntu (22.04.2 LTS)		
		Matlab R2022b (9.13)	
		SamSrf (9.51)	
		SPM12 (7771)	
Delineations (analysis and visualization)	Ubuntu (22.04.2 LTS)		
		Matlab R2022b (9.13)	
		SamSrf (9.51)	
PRF modeling (analysis and visualization)	Ubuntu (22.04.2 LTS)		
		Matlab R2022b (9.13)	
		SamSrf (9.51)	
		SPM12 (7771)	
		Scientific Colour Maps (8.0.0)[12]	
Simulations (analysis and visualization)	Ubuntu (22.04.2 LTS)		
		Matlab R2022b (9.13)	
		SamSrf (9.51)	
		SPM12 (7771)	
		Scientific Colour Maps (8.0.0)	
Insets (visualizations for intro and methods section)	Ubuntu (22.04.2 LTS)		
		Matlab R2022b (9.13)	
		SamSrf (9.51)	
		SPM12 (7771)	
		Scientific Colour Maps (8.0.0)	

Note. Reg. = regularization. Sampl. dist. = sampling distance. Trans. model = transformation model. Sim. metric = similarity metric. Trans. type = transformation type. MI = mutual information. PTB = Psychophysics Toolbox. SPM = Statistical Parametric Mapping. ANTs = Advanced Normalization Tools. SamSrf = Seriously Annoying Matlab Surfer. LTS = Long-term support. pRF = population receptive field. [1]The MathWorks Inc. (2015).[2]Brainard (1997), Kleiner et al. (2007), and Pelli (1997).[3]https://www.quaerosys.com/.[4]Rossum and Drake (2009).[5]Li et al. (2016).[6]Boré et al. (2021).[7]Dale et al. (1999), Fischl (2012), and Fischl et al. (1999).[8]The MathWorks Inc. (2022). [9]The FIL Methods Group (2021). [10]Tustison et al. (2021). [11]Schwarzkopf (2023). [12]Crameri (2023). Blank entries denote "not applicable".

Table S2

Median Cross-validated Goodness-of-fit (cR^2) as a Function of Participants/Simulation Type, Fitted pRF Model, and Cross-Validation Fold

	2dg-fix		onoff	
Participants/simulation type	odd on even	even on odd	odd on even	even on odd
Sub-01	0.39	0.35	0.36	0.32
Sub-02	0.54	0.60	0.50	0.55
Sub-03	0.20	0.20	0.19	0.21
$\text{Sim}_{\text{2dg-fix-accuracy-match}}$	0.55	0.55		
$\text{Sim}_{\text{2dg-fix-accuracy-mismatch}}$	0.55	0.55		
$\text{Sim}_{\text{onoff-cross-validated-goodness-of-fit}}$	0.54	0.54	0.54	0.54

Note. pRF = population receptive field. 2dg-fix = 2D Gaussian pRF model with parameter for pRF size fixed and constrained grid search. onoff = pRF model without any spatial tuning that simply reflects the presence or absence of tactile stimulation. odd(even) on even(odd) = odd(even) runs or simulated data validated on even(odd) runs or simulated data. $\text{Sim}_{\text{2dg-fix-accuracy-match}}$ = data were simulated using the 2dg-fix model for ground-truth pRFs matching the search grid value pairs to assess the computational validity (accuracy) of pRF estimates. $\text{Sim}_{\text{2dg-fix-accuracy-mismatch}}$ = just like $\text{Sim}_{\text{2dg-fix-accuracy-match}}$, but for ground-truth pRFs mismatching the search grid value pairs. $\text{Sim}_{\text{onoff-cross-validated-goodness-of-fit}}$ = data were simulated using the onoff model to assess the meaningfulness of differences in cross-validated goodness-of-fit. Blank entries denote "not applicable". Sub-01, Sub-02, Sub-03 = subject 01, 02, and 03.